
JOINT-EMBEDDING MASKED AUTOENCODER FOR SELF-SUPERVISED LEARNING OF DYNAMIC FUNCTIONAL CONNECTIVITY FROM THE HUMAN BRAIN

Jungwon Choi^{1*}  Hyungi Lee^{1*}  Byung-Hoon Kim^{2†}  Juho Lee^{1,3†} 

¹KAIST AI, Daejeon, South Korea

²Yonsei University College of Medicine, Seoul, South Korea

³AITRICS, Seoul, South Korea

ABSTRACT

Graph Neural Networks (GNNs) have shown promise in learning dynamic functional connectivity for distinguishing phenotypes from human brain networks. However, collecting large-scale labeled clinical data is often resource-intensive, limiting their practical use. This motivates the use of self-supervised learning to leverage abundant unlabeled data. While generative self-supervised approaches—particularly masked autoencoders—have shown promising results in representation learning in various domains, their application to dynamic graphs for dynamic functional connectivity remains underexplored and faces challenges in capturing high-level semantic patterns evolving over time. Here, we propose the Spatio-Temporal Joint Embedding Masked Autoencoder (ST-JEMA), which introduces a dual reconstruction objective that integrates spatial and temporal signals in dynamic brain graphs, enabling the encoder to learn temporally-aware semantic representations from unlabeled fMRI data. This design addresses key challenges in fMRI representation learning by capturing the spatio-temporal structure of dynamic functional connectivity. Unlike prior approaches that focus solely on static or spatial components, our method jointly reconstructs temporal dynamics and structural variations across time. Utilizing the large-scale UK Biobank dataset for self-supervised learning, ST-JEMA demonstrates robust representation learning performance across eight benchmark resting-state fMRI datasets, outperforming prior self-supervised methods in phenotype prediction and psychiatric diagnosis tasks—even with limited labeled data. Moreover, ST-JEMA proves resilient under temporal missing data scenarios, emphasizing the value of temporal reconstruction objectives. These findings demonstrate the effectiveness of our method for learning robust representations from fMRI data, particularly in label-scarce scenarios.

Keywords Functional connectivity · Dynamic brain networks · Spatiotemporal graph · Self-supervised learning · Representation learning

1 Introduction

Recent advancements in neuroimaging research have shown a growing interest in leveraging functional Magnetic Resonance Imaging (fMRI), which captures the Blood-Oxygen-Level-Dependent (BOLD) signal to understand the intricate functionalities of the human brain [1, 2]. Consequently, leveraging fMRI data through Functional Connectivity (FC) has gained traction in addressing various human brain-related problems using neural network models [3]. In this context, FC refers to the temporal correlation degree between Regions of Interest (ROI) of the brain, enabling the mathematical interpretation of fMRI data as graph structures, where nodes represent ROIs and edges represent the connectivity or correlation between these regions. This enables the utilization of graph-based learning methods such as Graph Neural Network (GNN) to analyze and interpret brain dynamics [4, 5].

*Equal contribution. †Corresponding authors: Juho Lee (juholee@kaist.ac.kr), Byung-Hoon Kim (egyptdj@yonsei.ac.kr)

While integrating GNN with FC data has marked significant advancements in understanding brain networks, obtaining and labeling clinical fMRI data for supervised learning models poses challenges, affecting the scalability and practical application of these advanced techniques. This challenge highlights the necessity of exploring alternative approaches capable of efficiently leveraging unlabeled data.

In response, utilizing unlabeled fMRI data through Self-Supervised Learning (SSL) presents a promising solution to extract valuable features for downstream tasks [6, 7, 8]. SSL, focused on pre-training backbone models without labels, has driven performance enhancements in diverse domains, including Natural Language Processing (NLP) [9], Image [10, 11], and Video Processing [12]. Among various SSL paradigms, generative approaches inspired by Masked Language Modeling (MLM) have shown superior performance compared to the contrastive learning methods in downstream tasks [11, 12] across a range of different tasks.

This trend has also emerged in graph domains, as demonstrated by GraphMAE [8], which applies a similar philosophy to static graphs and outperforms traditional contrastive SSL approaches. In the context of dynamic graphs, Choi et al. [13] have developed a generative SSL framework that enables foundational models to effectively capture temporal dynamics. When applied to fMRI datasets, this framework demonstrates enhanced performance across multiple downstream tasks, surpassing models based on static graph methodologies and contrastive learning approaches.

While recent advancements in generative SSL have shown improved performance in learning graph data structures, existing methods tend to focus on reconstructing lower-level features [8, 13], potentially limiting their ability to grasp higher-level semantic representations. Focusing on low-level features hinders the ability of the model to capture generalizable representations for downstream tasks.

To tackle this limitation of current generative SSL methods — reconstructing low-level representation in temporal graph data — we propose a novel framework called Spatio-Temporal Joint Embedding Masked Autoencoder (ST-JEMA) for dynamic graphs such as dynamic functional connectivity of fMRI data. In ST-JEMA, we propose a new joint embedding reconstruction loss based on the latest SSL frameworks known as Joint-Embedding Predictive Architecture (JEPa) [14]. The JEPa-inspired loss encourages the encoder to reconstruct latent representations rather than raw features, incorporating both spatial and temporal dimensions. This encourages the GNN models to learn more advanced representations of dynamic graphs.

We employed the extensive UK Biobank fMRI dataset, which consists of 40 913 records, for comparing various SSL methods without demographic characteristics (e.g. Gender), and validated our methodology by fine-tuning across eight benchmarks including non-clinical and clinical fMRI datasets. Experiments showed that ST-JEMA effectively improves node representation learning compared to baseline SSL methods. This improvement was evident in its superior performance on downstream fMRI tasks.

Our key contributions are outlined as follows:

- We propose ST-JEMA, a novel framework that shifts generative SSL from low-level feature reconstruction toward high-level representation learning in dynamic graphs.
- By employing the extensive fMRI data from the UKB dataset, we achieved enhanced performance across diverse benchmarks, thereby validating the effectiveness of our approach in using large-scale, unlabeled data for backbone GNN models.
- Our proposed method demonstrates enhanced efficacy in scenarios with limited labeled samples, such as with clinical datasets, notably in the data-efficient model development for psychiatric diagnosis classification.

2 Related Works

2.1 Learning Functional Connectivity of the Brain with Graph Neural Networks

Recent advances in GNNs have facilitated the modeling of brain networks using FC derived from fMRI data. Pioneering GNN-based approaches tackle the high-dimensional nature of fMRI by modeling brain dynamics [15], employing ROI-aware architectures [16], or introducing generative frameworks [17].

Contrary to the prevalent focus on static FC, there have been efforts to capture the temporal dynamics within fMRI data by proposing temporal dynamic learning [18], modeling temporal variants in brain networks [5], and combining graph structure learning with attention-based graph pooling [19], leveraging the rich temporal variation inherent to such dynamic brain networks. These studies consider temporal variation as an important part of analyzing the brain or determining disorders from fMRI data. In this work, we address the problem of enabling GNN encoders to learn the temporal dynamics inherent in large-scale unlabeled fMRI data by focusing on dynamic graphs.

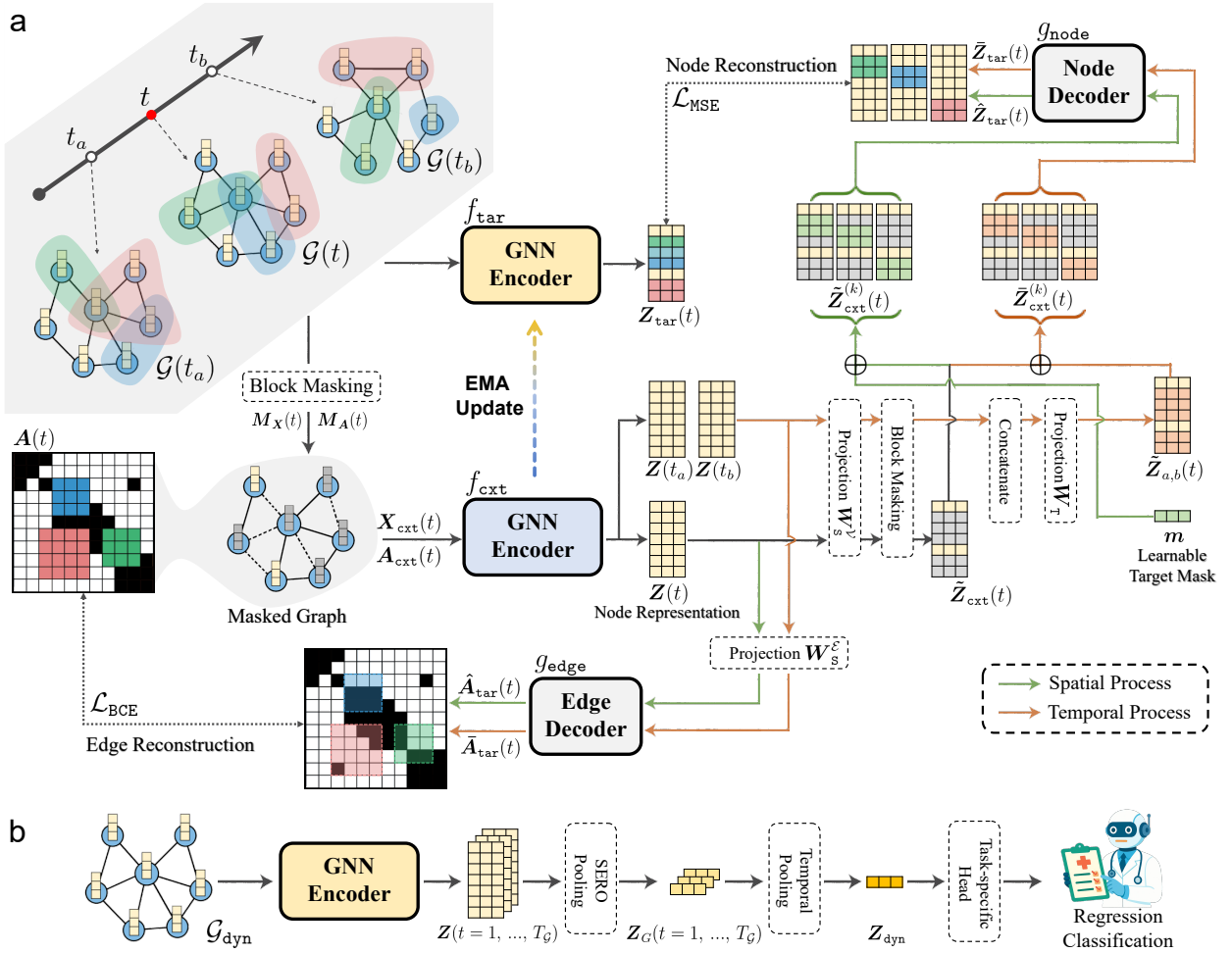


Figure 1: Overview of the Spatio-Temporal Joint Embedding Masked Autoencoder (ST-JEMA) framework. (a) Pre-training pipeline, where the model jointly reconstructs node representations and edge structures by masking blocks in both spatial and temporal dimensions. The context and target GNN encoders are updated via EMA. Spatial and temporal processes are indicated by green and orange dashed lines, respectively. (b) Fine-tuning pipeline for downstream tasks (classification or regression), where the pre-trained encoder outputs are pooled across spatial and temporal dimensions to generate task-specific representations.

2.2 Self-supervised Learning on Graph Data

SSL effectively extracts meaningful representations from large-scale unlabeled graph data. In the realm of graph contrastive SSL, Deep Graph Infomax [20] and GraphCL [6] have been pioneering efforts that leverage augmentations and multiple graph views to enrich representation learning. However, challenges in augmentation efficacy across domains have led to innovative works, which simplify the process by introducing perturbations to embeddings [21] or model parameters [7]. Generative approaches in graph self-supervised learning focus on reconstructing the original graph structure or node features from encoded representations to capture inherent structural relationships. VGAE [22] employs variational autoencoders for adjacency matrix reconstruction enhancing link prediction performance, while GraphMAE [8] employs a masked autoencoder approach, which shows enhanced performance in node and graph classification compared to previous contrastive methods.

Existing graph self-supervised learning methods are well-established for static graphs but remain less explored for dynamic graphs, especially in learning from dynamic FC, with existing applications mainly in other domains such as traffic flow [4]. Recently, a generative SSL framework designed for dynamic graphs from fMRI data, employing a masked autoencoder for temporal reconstruction, has shown promise in improving downstream task performance [13].

2.3 Joint Embedding Predictive Architecture

In the evolving landscape of SSL in computer vision, Assran et al. [14] introduces the JEPA, a new framework that integrates the concepts of both Joint Embedding Architecture (JEA) in contrastive learning and generative learning process of the Masked Autoencoder [MAE; 11]. This approach diverges from the MAE, which mainly focuses on pixel-level image reconstruction. Unlike MAE, which reconstructs masked patches, JEPA aims to avoid the potential pitfall of generating representations overly fixated on low-level details. Instead, Assran et al. [14] utilizes a predictive model trained to infer the representations of masked target patches based on unmasked context patches, enabling the encoder to formulate representations that encapsulate higher-level semantic information beyond mere pixel details.

Refer to Appendix G for more detailed discussions on the related works.

3 Preliminaries

3.1 Problem Definition

We aim to develop a SSL framework for capturing temporal dynamics in dynamic graphs constructed from large-scale, unlabeled fMRI data. We pre-train a GNN encoder $f(\cdot; \theta)$ and decoder $g(\cdot; \phi)$ using our SSL strategies, and discard the decoder during downstream fine-tuning with prediction heads $h(\cdot; \omega)$. The objective is to obtain an encoder $f(\cdot; \theta^*)$ that captures transferable representations captured the key patterns and dynamics within the fMRI data under limited supervision.

3.2 Dynamic Graph Construction from fMRI data

We represent fMRI-based brain activity as a dynamic graph sequence $\mathcal{G}(t) = (\mathcal{V}(t), \mathcal{E}(t))$ over discrete time $t \in \mathcal{T}$. Each node $i \in \mathcal{V}(t)$ corresponds to a brain region (ROI) defined by the Schaefer atlas [23], with N representing the number of ROIs. Each node is associated with a feature vector $\mathbf{x}_i(t) \in \mathbb{R}^{d_v}$. The node feature is defined as:

$$\mathbf{x}_i(t) = \mathbf{W}[e_i \parallel \boldsymbol{\eta}(t)], \quad (1)$$

where e_i is a spatial embedding and $\boldsymbol{\eta}(t)$ is a temporal encoding from a GRU [24] module.

Edges between nodes are defined using functional connectivity computed via the Pearson correlation of BOLD signals within a sliding temporal window:

$$R_{ij}(t) = \frac{\text{Cov}(\bar{\mathbf{p}}_i(t), \bar{\mathbf{p}}_j(t))}{\sqrt{\text{Var}(\bar{\mathbf{p}}_i(t))}\sqrt{\text{Var}(\bar{\mathbf{p}}_j(t))}} \in \mathbb{R}^{N \times N}, \quad (2)$$

The adjacency matrix $\mathbf{A}(t) \in \{0, 1\}^{N \times N}$ is then obtained by thresholding the top-30% of correlations. Further construction details are in Appendix B.

3.3 Context and Target for Reconstruction

Our method expands generative SSL by adapting the core idea of JEPA [14]—reconstructing latent representations instead of input features—into the domain of dynamic graphs derived from fMRI data. While JEPA operates on static image patches, we introduce a multi-block masking strategy suited to spatio-temporal brain graphs. Each graph $\mathcal{G}(t)$ is partially masked with K different binary masks, enabling learning from diverse context-target configurations.

Specifically, we define context and target node sets at time t as:

$$\begin{aligned} \mathbf{X}_{\text{cxt}}^{(k)}(t) &= \{\mathbf{x}_i(t) \mid i \in [N], \mathbf{M}_{\mathbf{X},i}^{(k)}(t) = \mathbf{1}_{d_v}\}, \\ \mathbf{X}_{\text{tar}}^{(k)}(t) &= \{\mathbf{x}_i(t) \mid i \in [N], \mathbf{M}_{\mathbf{X},i}^{(k)}(t) = \mathbf{0}_{d_v}\}, \end{aligned} \quad (3)$$

where $\mathbf{M}_{\mathbf{X}}^{(k)}(t) \in \{0, 1\}^{N \times d_v}$ is the k -th binary mask.

In parallel, we apply the same masking strategy to the adjacency matrices $\mathbf{A}(t)$, where masked edges are excluded from message passing and subsequently reconstructed using the contextual node embeddings. This allows the model to jointly learn node-level and connectivity-level representations in the latent space.

4 Methods

4.1 Joint Embedding Architecture

To enhance GNN encoder to capture higher-level semantic information in spatial and temporal patterns, we have introduced a new JEPA-inspired reconstruction strategy, utilizing dual encoders and decoders. The encoders, designated as $f_{\text{cxt}}(\cdot; \theta)$ for context and $f_{\text{tar}}(\cdot; \bar{\theta})$ for target, encode the context and target components, respectively, with θ representing the learnable parameters for the context encoder and $\bar{\theta}$ for the target encoder, which is updated based on θ . Meanwhile, the decoders, named $g_{\text{node}}(\cdot; \phi_{\mathcal{V}})$ and $g_{\text{edge}}(\cdot; \phi_{\mathcal{E}})$, aim to reconstruct the target nodes' representations and the adjacency matrix, respectively. Here, $\phi_{\mathcal{V}}$ and $\phi_{\mathcal{E}}$ denote the parameters of each decoder, respectively.

Employing separate encoders for context and target components is crucial to prevent representation collapse [25] during training [14]. Although these encoders share identical structural designs, they follow distinct parameter update rules. Specifically, the context encoder f_{cxt} is updated via Stochastic Gradient Descent (SGD), driven by subsequent reconstruction loss objectives, while the target encoder f_{tar} remains frozen.

Subsequently, The parameters of target encoder, $\bar{\theta}$, are then updated using Exponential Moving Average (EMA) based on the evolving parameters of f_{cxt} as follows:

$$\bar{\theta}_{\text{new}} = \beta \bar{\theta}_{\text{old}} + (1 - \beta) \theta_{\text{cxt}}, \quad (4)$$

where hyperparameter $\beta \in [0, 1]$ represents the decay factor. Here, $\bar{\theta}_{\text{old}}$ and $\bar{\theta}_{\text{new}}$ refer to the parameters of f_{tar} before and after applying EMA process, respectively, and θ_{cxt} indicates the current parameters of f_{cxt} . Adopting distinct update rules for each encoder helps avoid simplistic and non-informative trivial representations. This approach allows us to harness GNN encoder to learn high-level semantic representations while maintaining nearly the same computational demand during back-propagation.

4.2 Block Masking Process for Masked Autoencoding

To effectively train spatial and temporal patterns across individual time steps t , suitable masks need to be applied to both the node features and the adjacency matrix $(\mathbf{X}(t), \mathbf{A}(t))$, resulting in masked versions $(\mathbf{X}_{\text{cxt}}(t), \mathbf{A}_{\text{cxt}}(t))$ for each time step t .

As presented in Assran et al. [14], when training a model with a JEPA-based masked autoencoding objective, a sufficiently large size of the target masks, with sequential indices, is crucial in the image dataset. This strategy ensures that the masked targets encompass meaningful semantic information, allowing models to grasp the semantic structure by reconstructing the target data from the remaining context. While patch-based masking is straightforward for images, applying similar masking techniques to nodes and edges in graph data is challenging due to the absence of clear relationships between sequential indices for nodes. However, in the context of dynamic FC of fMRI data, the graph construction method outlined in Kim et al. [5] defines a well-aligned construction between nodes with adjacent indices across time. Consequently, masking nodes with sequential indices is a natural and effective approach for the dynamic FC of fMRI data. This method allows for the masking of nodes without sacrificing meaningful semantic information.

As mentioned earlier, generating adequately sized masks for both nodes and edges at each time step t is essential to capture meaningful semantic information within the masked blocks. To achieve this for node features $\mathbf{X}(t)$, we generate K binary mask matrices $\mathbf{M}_{\mathbf{X}}^{(k)}(t)$, where each $\mathbf{M}_{\mathbf{X}}^{(k)}(t)$ randomly and independently masks a $\lfloor \alpha_{\text{node}}^{(k)}(t) \cdot N \rfloor$ number of nodes with sequential indices. Here, mask ratio $\alpha_{\text{node}}^{(k)}(t)$ uniformly sampled from $(\alpha_{\text{min}}, \alpha_{\text{max}})$ where $0 < \alpha_{\text{min}} < \alpha_{\text{max}} < 1$ are predefined hyperparameters. This process ensures the creation of appropriately sized blocks. Refer to Appendix F.5 for the experimental results regarding the ablation study on block mask ratios.

After generating K distinct masks, when creating context node features for each target node feature, the memory requirements for context node features increase linearly with the growth of K . To remedy this issue, we employ a single global context node feature for each time t , outlined as follows:

$$\mathbf{X}_{\text{cxt}}(t) = \mathbf{X}(t) \odot \bigcap_{k=1}^K \mathbf{M}_{\mathbf{X}}^{(k)}(t), \quad (5)$$

where \odot denotes element-wise (Hadamard) product and \bigcap denotes element-wise logical AND over binary matrices.

For the adjacency matrix $\mathbf{A}(t)$, we also construct K binary masks $\mathbf{M}_{\mathbf{A}}^{(k)}(t)$ for $k \in [K]$ in a similar fashion. The distinction in constructing an adjacency matrix mask primarily involves blocking a randomly chosen square-shaped submatrix. To create a mask $\mathbf{M}_{\mathbf{A}}^{(k)}(t)$ by sampling a square-shaped submatrix from the adjacency matrix, we independently

and randomly select two sets of sequential indices I_1 and I_2 . These sets have the same cardinality of $\lfloor \alpha_{\text{adj}}^{(k)}(t) \cdot N \rfloor$, where $\alpha_{\text{adj}}^{(k)}(t)$ is uniformly sampled from $(\alpha_{\text{min}}, \alpha_{\text{max}})$. Subsequently, we nullify the (i, j) th entry of $M_A^{(k)}(t)$ for all $i \in I_1$ and $j \in I_2$. Following the independent and random construction of K adjacency matrix masks, akin to node features, we utilize a single global context adjacency matrix for each time t , described as follows:

$$\mathbf{A}_{\text{cxt}}(t) = \mathbf{A}(t) \odot \bigcap_{k=1}^K M_A^{(k)}(t), \quad (6)$$

The aforementioned masking strategies for the node features and the adjacency matrix encourage the model to learn the underlying brain connectivity patterns for each time t thereby enhancing the understanding of dynamics in the spatial dimension.

4.3 Spatial Reconstruction Process

Based on the masks generated from Section 4.2, we introduce an objective function inspired by JEPA, referred to as $\mathcal{L}_{\text{spat}}$, aiming to facilitate the learning of spatial patterns within the dynamic FC of fMRI data using GNN representations. To create $\mathcal{L}_{\text{spat}}$, we need to reconstruct the target node representations and the target adjacency matrix based on the context node representations and the context adjacency matrix. To achieve this reconstruction, we initially build the common context node representation for each time t as follows:

$$\mathbf{Z}(t) = f_{\text{cxt}}(\mathbf{X}_{\text{cxt}}(t), \mathbf{A}_{\text{cxt}}(t); \boldsymbol{\theta}). \quad (7)$$

Here, we can employ any GNN models capable of accepting node features and adjacency matrices as input for our f_{cxt} . To reconstruct the target node representations using only the context node representations, we reapply masking to the context node representations at the indices corresponding to the masked target node representations. This results in generating masked context node representations $\tilde{\mathbf{Z}}_{\text{cxt}}(t)$ computed as follows:

$$\begin{aligned} \tilde{\mathbf{Z}}(t) &= \mathbf{W}_s^{\mathcal{V}} \mathbf{Z}(t), \\ \tilde{\mathbf{Z}}_{\text{cxt}}(t) &= \tilde{\mathbf{Z}}(t) \odot \bigcap_{k=1}^K M_X^{(k)}(t), \end{aligned} \quad (8)$$

where $\mathbf{W}_s^{\mathcal{V}} \in \mathbb{R}^{d_{\text{dec}} \times d_{\text{enc}}}$ projects encoder outputs to decoder space. Using the masked context node representations $\tilde{\mathbf{Z}}(t)$ and any node mask $M_X^{(k)}(t)$, we derive the target-specific context node representations $\tilde{\mathbf{Z}}_{\text{cxt}}^{(k)}(t)$ as follows:

$$\tilde{\mathbf{Z}}_{\text{cxt}}^{(k)}(t) = \tilde{\mathbf{Z}}_{\text{cxt}}(t) + \mathbf{m} \cdot (\mathbf{1}_X - M_X^{(k)}(t)), \quad (9)$$

where $\mathbf{1}_X$ represents a matrix filled with ones having the same shape as $M_X^{(k)}(t)$, and $\mathbf{m} \in \mathbb{R}^{d_{\text{dec}}}$ denotes a learnable mask vector conditioning the target block we wish to reconstruct following Assran et al. [14]. This vector is crucial for conditioning the specific target block among K mask blocks from the single global context node representation $\tilde{\mathbf{Z}}_{\text{cxt}}(t)$.

In summary, these target-specific context node representations $\tilde{\mathbf{Z}}_{\text{cxt}}^{(k)}(t)$ are set to zero for all target node representations belonging to $K - 1$ masks, except for those associated with the k -th mask. For the latter, corresponding representations are set to the values from the learnable mask vector \mathbf{m} . Then finally with this target-specific context node representation $\tilde{\mathbf{Z}}_{\text{cxt}}^{(k)}(t)$, we recover the target node representation $\hat{\mathbf{Z}}_{\text{tar}}^{(k)}(t)$ for the k -th mask as follows:

$$\hat{\mathbf{Z}}_{\text{tar}}^{(k)}(t) = g_{\text{node}}(\tilde{\mathbf{Z}}_{\text{cxt}}^{(k)}(t); \phi_{\mathcal{V}}). \quad (10)$$

For the architecture of g_{node} , we opt for the MLP-Mixer [26] architecture. This choice is different from the usual selection of a Multi-Layer Perceptron (MLP) as the decoder for the graph SSL. In contrast to a simple MLP structure, the MLP-Mixer structure facilitates interactions among all nodes, enabling the reconstruction of the target node's representation by fully considering the representations of context nodes.

Our target node representations for the k -th mask $\mathbf{Z}_{\text{tar}}^{(k)}(t)$ is computed with unmasked $\mathbf{X}(t)$ and $\mathbf{A}(t)$:

$$\begin{aligned}\mathbf{Z}_{\text{tar}}(t) &= f_{\text{tar}}\left(\mathbf{X}(t), \mathbf{A}(t); \bar{\boldsymbol{\theta}}\right), \\ \mathbf{Z}_{\text{tar}}^{(k)}(t) &= \mathbf{Z}_{\text{tar}}(t) \odot \left(\mathbf{1}_{\mathbf{X}} - \mathbf{M}_{\mathbf{X}}^{(k)}(t)\right).\end{aligned}\quad (11)$$

Then finally our node reconstruction objective $\mathcal{L}_{\text{node-spat}}^{(t)}$ at time t is computed as follows:

$$\mathcal{L}_{\text{node-spat}}^{(t)} = \frac{1}{K} \sum_{k \in [K]} \mathcal{L}_{\text{MSE}}\left(\hat{\mathbf{Z}}_{\text{tar}}^{(k)}(t), \mathbf{Z}_{\text{tar}}^{(k)}(t)\right), \quad (12)$$

where \mathcal{L}_{MSE} denotes the Mean Squared Error (MSE) loss. In contrast to prior graph-based MAE methods [8, 27], where the entire node representations are recovered by the decoder module, our approach only focuses on recovering the target node representations. This encourages the model to focus on semantic information embedded within the masked target nodes.

To recover the adjacency matrix at time t , we used the common context node representation $\mathbf{Z}(t)$. Based on the reconstruction approach in Kipf and Welling [22], our reconstructed target adjacency matrix $\hat{\mathbf{A}}_{\text{tar}}^{(k)}(t)$ for the k -th mask $\mathbf{M}_{\mathbf{A}}^{(k)}(t)$ at time t computed as follows:

$$\begin{aligned}\mathbf{H}(t) &= g_{\text{edge}}\left(\mathbf{W}_{\text{S}}^{\mathcal{E}} \mathbf{Z}(t); \phi_{\mathcal{E}}\right), \\ \hat{\mathbf{A}}_{\text{tar}}^{(k)}(t) &= \text{sig}\left(\mathbf{H}(t)\mathbf{H}(t)^{\top}\right) \odot \left(\mathbf{1}_{\mathbf{A}} - \mathbf{M}_{\mathbf{A}}^{(k)}(t)\right),\end{aligned}\quad (13)$$

where $\mathbf{1}_{\mathbf{A}}$ represents a matrix filled with ones having the same shape as $\mathbf{M}_{\mathbf{A}}^{(k)}(t)$, and sig is an element-wise sigmoid function. We also apply a learnable projection matrix $\mathbf{W}_{\text{S}}^{\mathcal{E}} \in \mathbb{R}^{d_{\text{dec}} \times d_{\text{enc}}}$ to adjust dimensions from the encoder to the decoder. And our target adjacency submatrix $\mathbf{A}_{\text{tar}}^{(k)}(t)$ for the k -th mask at time t is simply computed as:

$$\mathbf{A}_{\text{tar}}^{(k)}(t) = \mathbf{A}(t) \odot \left(\mathbf{1}_{\mathbf{A}} - \mathbf{M}_{\mathbf{A}}^{(k)}(t)\right). \quad (14)$$

Then our adjacency matrix reconstruction loss $\mathcal{L}_{\text{adj-spat}}^{(t)}$ at time t is computed as follows:

$$\mathcal{L}_{\text{adj-spat}}^{(t)} = \frac{1}{K} \sum_{k \in [K]} \mathcal{L}_{\text{BCE}}\left(\hat{\mathbf{A}}_{\text{tar}}^{(k)}(t), \mathbf{A}_{\text{tar}}^{(k)}(t)\right), \quad (15)$$

where \mathcal{L}_{BCE} denote the Binary Cross-Entropy (BCE) loss function.

In summary, our overall loss function $\mathcal{L}_{\text{spat}}$ to capture and learn the spatial patterns is formulated as:

$$\mathcal{L}_{\text{spat}} = \sum_{t \in \mathcal{T}} \left(\lambda_{\text{node}} \mathcal{L}_{\text{node-spat}}^{(t)} + \lambda_{\text{adj}} \mathcal{L}_{\text{adj-spat}}^{(t)} \right), \quad (16)$$

where λ_{node} and λ_{adj} serve as hyperparameters regulating the scales of the two individual loss terms.

4.4 Temporal Reconstruction Process

To enhance the understanding of temporal dynamics within the dynamic FC of fMRI data, we also construct a JEPA-based $\mathcal{L}_{\text{temp}}$. This temporal reconstruction strategy is designed to predict node representations and adjacency matrices at a specific time t by utilizing node representation from two random points in time, t_a and t_b , that can encompass t within their interval. For the selection of t_a and t_b , we adopt a uniform sampling strategy following Choi et al. [13], a straightforward method for choosing two temporal points. An important consideration when sampling t_a and t_b is the use of a temporal windowing process with a length of Γ and a stride of S when constructing a series of FC matrices from the BOLD signal, as discussed in Appendix B. If t_a and t_b are sampled too closely, there may be an overlap between the windows of t_a and t_b , making the reconstruction task trivial. To ensure the challenge and effectiveness of the temporal reconstruction task, we take care to ensure that the sampled time points t_a and t_b do not originate from overlapping windows as follows:

$$t_a \stackrel{\text{i.i.d.}}{\sim} U_{\text{int}}([0, t - d_{\text{min}}]), \quad t_b \stackrel{\text{i.i.d.}}{\sim} U_{\text{int}}([t + d_{\text{min}}, T_{\mathcal{G}}]), \quad (17)$$

where t is a target timestep, $U_{\text{int}}(I)$ is a uniform distribution for all integer values in interval I and $d_{\text{min}} = \frac{1}{2}(\frac{\Gamma}{S} + 1)$.

Then we first reconstruct the target node representations $\bar{\mathbf{Z}}_{\text{tar}}^{(k)}(t)$ for the k -th mask at time t utilizing $\mathbf{Z}(t_a)$ and $\mathbf{Z}(t_b)$ which are the context node representation at time t_a and time t_b , respectively. To aggregate $\mathbf{Z}(t_a)$ and $\mathbf{Z}(t_b)$ into single node representation $\tilde{\mathbf{Z}}_{a,b}(t)$, we compute the $\tilde{\mathbf{Z}}_{a,b}(t)$ as follows:

$$\tilde{\mathbf{Z}}_{a,b}(t) = \mathbf{W}_{\text{T}} \left[\tilde{\mathbf{Z}}(t_a) \parallel \tilde{\mathbf{Z}}(t_b) \right], \quad (18)$$

where, $\mathbf{W}_{\text{T}} \in \mathbb{R}^{d_{\text{dec}} \times 2d_{\text{enc}}}$ denotes a learnable projection matrix. Instead of employing a learnable mask vector to fill the masked target node representations at $\tilde{\mathbf{Z}}(t)$, as described in Eq. (9), we utilize node representations from t_a and t_b to construct the target-specific context node representations $\bar{\mathbf{Z}}_{\text{cxt}}^{(k)}(t)$ for the k -th mask at time t as follows:

$$\bar{\mathbf{Z}}_{\text{cxt}}^{(k)}(t) = \tilde{\mathbf{Z}}_{\text{cxt}}(t) + \tilde{\mathbf{Z}}_{a,b}(t) \odot \left(\mathbf{1}_{\mathbf{X}} - \mathbf{M}_{\mathbf{X}}^{(k)}(t) \right). \quad (19)$$

Employing $\tilde{\mathbf{Z}}_{a,b}(t)$ to populate the target node representations helps the model capture temporal dynamics more effectively, enhancing its understanding of temporal variations. The recovered target node representations are obtained using the same decoder g_{node} as in the spatial task:

$$\bar{\mathbf{Z}}_{\text{tar}}^{(k)}(t) = g_{\text{node}} \left(\bar{\mathbf{Z}}_{\text{cxt}}^{(k)}(t); \phi_{\mathcal{V}} \right). \quad (20)$$

Our temporal node reconstruction loss $\mathcal{L}_{\text{node-temp}}^{(t)}$ at time t is computed as:

$$\mathcal{L}_{\text{node-temp}}^{(t)} = \frac{1}{K} \sum_{k \in [K]} \mathcal{L}_{\text{MSE}} \left(\bar{\mathbf{Z}}_{\text{tar}}^{(k)}(t), \mathbf{Z}_{\text{tar}}^{(k)}(t) \right). \quad (21)$$

For the adjacency matrix reconstruction task, we use $\mathbf{Z}(t_a)$ and $\mathbf{Z}(t_b)$ in different ways from the spatial reconstruction. We first construct each $\mathbf{H}(t_a)$ and $\mathbf{H}(t_b)$ using $\mathbf{Z}(t_a)$ and $\mathbf{Z}(t_b)$, respectively. Then compute the reconstructed adjacency matrix for time t as:

$$\bar{\mathbf{A}}_{\text{tar}}(t) = \frac{1}{2} \left(\text{sig}(\tilde{\mathbf{A}}_{ab}) + \text{sig}(\tilde{\mathbf{A}}_{ba}) \right), \quad (22)$$

where $\tilde{\mathbf{A}}_{ab} = \mathbf{H}(t_a)\mathbf{H}(t_b)^\top$ and $\tilde{\mathbf{A}}_{ba} = \mathbf{H}(t_b)\mathbf{H}(t_a)^\top$. Utilizing matrix multiplication between $\mathbf{H}(t_a)$ and $\mathbf{H}(t_b)$ to reconstruct the adjacency matrix also aids our model in effectively learning complex temporal dynamics within dynamic graph data [13].

Our reconstructed target adjacency submatrix $\bar{\mathbf{A}}_{\text{tar}}^{(k)}(t)$ for the k -th mask at time t formulated as:

$$\bar{\mathbf{A}}_{\text{tar}}^{(k)}(t) = \bar{\mathbf{A}}_{\text{tar}}(t) \odot \left(\mathbf{1}_{\mathbf{A}} - \mathbf{M}_{\mathbf{A}}^{(k)}(t) \right). \quad (23)$$

Therefore our temporal adjacency matrix reconstruction loss $\mathcal{L}_{\text{adj-temp}}^{(t)}$ can be computed as follows:

$$\mathcal{L}_{\text{adj-temp}}^{(t)} = \frac{1}{K} \sum_{k \in [K]} \mathcal{L}_{\text{BCE}} \left(\bar{\mathbf{A}}_{\text{tar}}^{(k)}(t), \mathbf{A}_{\text{tar}}^{(k)}(t) \right), \quad (24)$$

In summary, our overall loss function $\mathcal{L}_{\text{temp}}$ to understand the temporal patterns is formulated as:

$$\mathcal{L}_{\text{temp}} = \sum_{t \in \mathcal{T}} \left(\lambda_{\text{node}} \mathcal{L}_{\text{node-temp}}^{(t)} + \lambda_{\text{adj}} \mathcal{L}_{\text{adj-temp}}^{(t)} \right). \quad (25)$$

Here, we use same λ_{node} and λ_{adj} within $\mathcal{L}_{\text{spat}}$.

4.5 Summary of the Overall ST-JEMA Pipeline

During each training step, we calculate both the spatial reconstruction loss, $\mathcal{L}_{\text{spat}}$, and the temporal reconstruction loss, $\mathcal{L}_{\text{temp}}$. These two distinct loss components are then aggregated to formulate the combined objective function, $\mathcal{L}_{\text{ST-JEMA}}$, as follows:

$$\mathcal{L}_{\text{ST-JEMA}} = \gamma \mathcal{L}_{\text{spat}} + (1 - \gamma) \mathcal{L}_{\text{temp}}, \quad (26)$$

where the hyperparameter $\gamma \in [0, 1]$ is the ratio of $\mathcal{L}_{\text{spat}}$. The overview and complete training pipeline of the ST-JEMA are described in Fig. 1 and Appendix A.

Table 1: Gender classification performance across various downstream fMRI datasets. The performance is evaluated using the AUROC score, with higher scores indicating better performance.

Type of FC	Pre-training	Method Type	AUROC (\uparrow)								Rank
			ABCD	HCP-YA	HCP-A	HCP-D	HCP-EP	ABIDE	ADHD200	COBRE	
Static	Random-Init	Supervised	72.74	86.93	68.48	66.22	55.54	69.62	63.16	62.94	8.00
	DGI	Contrastive SSL	72.79	87.16	68.61	68.63	54.19	70.08	61.64	68.76	6.38
	SimGRACE		72.58	86.70	67.79	67.12	57.11	69.01	61.53	65.69	8.62
	GAE	Generative SSL	73.00	87.01	68.43	68.31	58.15	70.21	63.60	66.62	5.88
	VGAE		72.87	86.70	67.57	66.44	56.25	69.99	62.63	66.73	7.75
	GraphMAE		71.72	86.82	67.43	67.22	58.83	68.47	61.54	68.89	7.62
Dynamic	Random-Init	Supervised	<u>83.17</u>	92.54	83.18	73.30	58.41	72.95	<u>71.25</u>	<u>72.54</u>	3.12
	ST-DGI	Contrastive SSL	81.69	93.37	<u>84.99</u>	72.70	58.15	<u>74.87</u>	68.04	71.77	3.38
	ST-MAE	Generative SSL	82.78	<u>93.71</u>	84.34	<u>74.11</u>	<u>60.49</u>	74.74	71.01	67.80	<u>3.00</u>
	ST-JEMA (Ours)		84.16	93.99	85.65	74.97	63.58	75.38	71.94	80.61	1.00

Table 2: Age regression performance across various downstream fMRI datasets. Performance is evaluated using the MAE score, with lower scores indicating better performance.

Type of FC	Pre-training	Method Type	MAE (\downarrow)								Rank
			ABCD	HCP-YA	HCP-A	HCP-D	HCP-EP	ABIDE	ADHD200	COBRE	
Static	Random-Init	Supervised	6.45	3.11	9.38	2.51	3.33	4.35	2.04	9.81	9.38
	DGI	Contrastive SSL	6.45	3.05	9.29	2.43	3.21	4.24	2.02	9.59	6.12
	SimGRACE		6.44	3.08	9.27	2.45	3.29	4.34	2.03	9.74	7.12
	GAE	Generative SSL	6.44	3.10	9.21	2.44	3.18	4.28	2.03	9.70	6.38
	VGAE		6.44	3.13	9.37	2.45	3.21	4.25	2.02	9.40	6.62
	GraphMAE		6.44	3.05	9.35	2.49	3.17	4.40	2.01	9.55	6.38
Dynamic	Random-Init	Supervised	6.61	<u>2.78</u>	8.04	2.13	<u>2.94</u>	<u>4.10</u>	<u>1.90</u>	8.79	3.50
	ST-DGI	Contrastive SSL	6.45	<u>2.78</u>	<u>8.01</u>	<u>2.10</u>	2.96	4.16	1.91	9.16	3.50
	ST-MAE	Generative SSL	<u>6.43</u>	2.82	8.37	2.13	3.13	<u>4.10</u>	1.86	<u>8.76</u>	<u>2.75</u>
	ST-JEMA (Ours)		6.42	2.73	7.94	2.09	2.92	4.08	1.86	8.60	1.00

5 Experimental Setup

We utilize the UK Biobank [28] as the upstream dataset, a large-scale fMRI data comprised of 40 913 subjects, for pre-training GNN encoder with SSL. We evaluate the pre-trained GNN encoder across eight downstream datasets both non-clinical and clinical rs-fMRI datasets. For non-clinical datasets, we evaluate gender classification and age regression tasks using ABCD [29], and three types of HCP datasets: HCP-YA [30], HCP-A [31], and HCP-D [32]. For clinical datasets, we extended psychiatric diagnosis classification tasks to distinguish between normal control groups and different psychiatric disorder groups using HCP-EP [33], ABIDE [34], ADHD200 [35], and COBRE [36].

To show effectiveness of ST-JEMA, we compared these downstream performance against previous SSL methods including both static graphs (DGI [20], SimGRACE [7], GAE [22], VGAE [22], GraphMAE [8]) and dynamic graphs (ST-DGI [37], ST-MAE [13]).

The training process was divided into two phases: 1) pre-training, where a GNN encoder $f(\cdot; \theta)$ and decoder $g(\cdot; \phi)$ were learned using SSL on the UKB dataset without phenotype labels, employing a 4-layer GIN [38] for encoder module and a one-layer MLP-mixer for the decoder in the ST-JEMA framework, and 2) fine-tuning, where the pre-trained encoder and a task-specific head $h(\cdot; \omega)$, incorporating the SERO readout module [5], were further trained on downstream tasks with supervised learning.

Further details on the experimental setup are provided in the dataset specifications (Appendix C), baseline descriptions (Appendix D), and training configurations (Appendix E).

6 Results

6.1 Downstream-task Performance

6.1.1 Gender Classification

In gender classification tasks using the gender class phenotype from benchmark datasets, our proposed method, ST-JEMA, demonstrates superior AUROC performance across all benchmarks as shown in Table 1. Notably, it proved

Table 3: Psychiatric diagnosis classification performance on clinical fMRI datasets. The performance is evaluated using the AUROC score, with higher scores indicating better performance.

Type of FC	Pre-training	Method Type	AUROC (\uparrow)				Rank
			HCP-EP	ABIDE	ADHD200	COBRE	
Static	Random-Init	Supervised	67.47	63.04	55.44	57.86	8.75
	DGI	Contrastive SSL	67.13	64.30	56.55	62.09	6.00
	SimGRACE		64.41	64.54	58.25	61.50	5.75
	GAE		68.74	64.52	56.28	64.00	4.75
	VGAE	Generative SSL	66.79	64.32	55.74	61.74	7.25
	GraphMAE		63.67	64.22	55.78	63.48	7.25
Dynamic	Random-Init	Supervised	74.15	67.16	55.37	60.98	6.75
	ST-DGI	Contrastive SSL	77.78	68.86	56.46	61.08	4.75
	ST-MAE	Generative SSL	78.66	69.73	56.77	62.19	2.75
	ST-JEMA (Ours)		79.22	71.49	58.89	70.04	1.00

especially effective in classifying gender from clinical datasets, which typically comprise fewer samples than non-clinical datasets. We noted that employing dynamic rather than static FC resulted in performance improvements when comparing the overall performance of static and dynamic methods. This outcome proves the significance of considering temporal variations in gender classification tasks. Additionally, ST-JEMA outperformed previous dynamic graph self-supervised learning methods. This enhancement in performance shows that ST-JEMA has effectively learned representations that capture the temporal dynamics in the upstream rs-fMRI data.

6.1.2 Age Regression

In the age regression task, ST-JEMA consistently surpassed other methods in prediction accuracy across the most of datasets. The evaluation metric scales vary due to different age ranges in each dataset, refer to Table 2. Interestingly, the performance of the GNN encoder trained via ST-DGI was similar to, or in some instances worse than, the Dynamic Random-Init method, especially in clinical datasets that have fewer samples. Contrastive methods like ST-DGI showed unstable results, while ST-JEMA showed improved performance even in clinical data, suggesting that the representations learned through our methodology were more effective in distinguishing phenotypes.

6.1.3 Psychiatric Diagnosis Classification

The motivation behind employing SSL with a large amount of unlabeled fMRI data is to improve the performance of the downstream diagnosis classification task, typically constrained by a limited number of labeled training datasets. The GNN encoder is expected to learn the structure of fMRI data during upstream training, enabling better psychiatric classification with minimal clinical data. As shown in Table 3, in most cases, SSL-trained model showed better performance than those initialized randomly, proving that learning representations from unlabeled data is beneficial for accurately detecting signal variations in BOLD signals for psychiatric diagnosis classification. ST-JEMA notably surpassed other methods in psychiatric diagnosis classification, especially demonstrating significantly higher AUROC in the COBRE dataset, even when tasked with distinguishing between three distinct psychiatric conditions and control groups.

We further evaluated the versatility of representations learned by ST-JEMA through linear probing, multi-task learning, and temporal missing data scenarios. These results support the robustness of our model across diverse settings. See Appendix F for details.

6.2 Ablation Study

6.2.1 Fine-tuning Performance with Limited Samples

Clinical fMRI datasets often suffer from limited labeled data, which hinders the training of robust models. To assess the effectiveness of our pre-trained GNN under such constraints, we conducted experiments on 10%, 20%, 30%, and 50% subsets of the ABIDE dataset. and compared ST-JEMA with other dynamic graph SSL methods on psychiatric diagnosis classification. As shown in Fig. 2, ST-JEMA consistently outperformed all baselines, even with as little as 20% of the training data, indicating its ability to learn semantic representations beneficial under data scarcity. Notably, ST-DGI failed to surpass Random-Init when using less than 50%, revealing the limitations of contrastive-based methods.

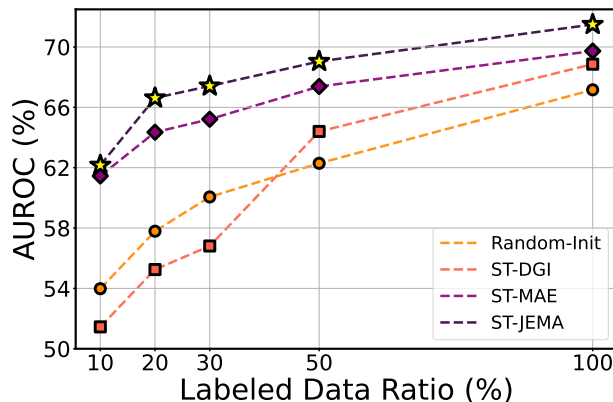


Figure 2: Ablation study on the impact of limited labeled samples for the diagnosis classification task. We fine-tuned the pre-trained GNN model using a limited number of samples, randomly sampled from the ABIDE dataset.

Table 4: Ablation results on reconstruction losses in $\mathcal{L}_{\text{ST-JEMA}}$. Baseline (1)–(4) node, edge, spatial, and temporal loss components, respectively.

Method	Node	Edge	$\mathcal{L}_{\text{spatial}}$	$\mathcal{L}_{\text{temporal}}$	AUROC (\uparrow)
Random Init	✗	✗	✗	✗	67.16
Baseline (1)	✗	✓	✓	✓	68.24
Baseline (2)	✓	✗	✓	✓	70.33
Baseline (3)	✓	✓	✗	✓	69.79
Baseline (4)	✓	✓	✓	✗	65.19
ST-JEMA (Ours)	✓	✓	✓	✓	71.49

These results demonstrate the effectiveness of generative SSL for clinical neuroimaging tasks where labeled data is scarce.

6.2.2 Ablation on Loss Function

In formulating the loss $\mathcal{L}_{\text{ST-JEMA}}$, we consider four key components: 1) node representation reconstruction, 2) edge reconstruction, 3) spatial, and 4) temporal objectives. We evaluate their contributions through an ablation study on the psychiatric diagnosis classification task using the ABIDE dataset. Table 4 clearly shows that excluding any loss term from $\mathcal{L}_{\text{ST-JEMA}}$ results in a significant drop in performance compared to ST-JEMA. Notably, the most substantial performance decline is observed when excluding the temporal loss $\mathcal{L}_{\text{temp}}$, highlighting the critical importance of capturing temporal dynamics in fMRI data for accurately addressing downstream tasks. Meanwhile, the performance of baselines, except when excluding the temporal loss, consistently outperforms the Random Init baseline. This demonstrates the significance of pre-training on a large upstream dataset, particularly in scenarios where the downstream data is limited in terms of labeled samples, as commonly encountered in clinical fMRI datasets.

Refer to Appendix F to see further ablation experiments on the impact of pre-training data size, block mask ratio, and decoder architecture.

7 Conclusion

We introduced Spatio-Temporal Joint-Embedding Masked Autoencoder (ST-JEMA), SSL framework tailored for fMRI data. Leveraging the JEPA [14] framework, ST-JEMA captures both spatial and temporal dynamics in the dynamic FC of fMRI data by jointly optimizing spatial and temporal reconstruction objectives. Extensive experiments on both non-clinical and clinical downstream tasks demonstrate that our method outperforms existing SSL approaches across classification and regression tasks. These findings highlight the effectiveness of ST-JEMA in learning robust representations from unlabeled fMRI data, particularly in data-constrained scenarios common in neuroimaging research.

Acknowledgments

We would like to thank Sungho Keum for his valuable discussions that contributed to the development of this work. This research was partly supported by Basic Science Research Program through the National Research Foundation of Korea (NRF) funded by the Ministry of Education (NRF-2022R111A1A01069589), National Research Foundation of Korea(NRF) grant funded by the Korea government(MSIT) (NRF-2021M3E5D9025030), Institute of Information & communications Technology Planning & Evaluation (IITP) grant funded by the Korea government(MSIT) (No.2019-0-00075, Artificial Intelligence Graduate School Program(KAIST), No.2022-0-00713, Meta-learning Applicable to Real-world Problems).

References

- [1] Meenakshi Khosla, Keith Jamison, Amy Kuceyeski, and Mert R Sabuncu. 3d convolutional neural networks for classification of functional connectomes. In *International Workshop on Deep Learning in Medical Image Analysis*, pages 137–145. Springer, 2018.
- [2] Xin Yang, Mohammad Samiul Islam, and AM Arefin Khaled. Functional connectivity magnetic resonance imaging classification of autism spectrum disorder using the multisite abide dataset. In *2019 IEEE EMBS International Conference on Biomedical & Health Informatics (BHI)*, pages 1–4. IEEE, 2019.
- [3] Byung-Hoon Kim and Jong Chul Ye. Understanding graph isomorphism network for rs-fmri functional connectivity analysis. *Frontiers in neuroscience*, 14:630, 2020.
- [4] Soham Gadgil, Qingyu Zhao, Adolf Pfefferbaum, Edith V Sullivan, Ehsan Adeli, and Kilian M Pohl. Spatio-temporal graph convolution for resting-state fmri analysis. In *Medical Image Computing and Computer Assisted Intervention–MICCAI 2020: 23rd International Conference, Lima, Peru, October 4–8, 2020, Proceedings, Part VII 23*, pages 528–538. Springer, 2020.
- [5] Byung-Hoon Kim, Jong Chul Ye, and Jae-Jin Kim. Learning dynamic graph representation of brain connectome with spatio-temporal attention. *Advances in Neural Information Processing Systems*, 34:4314–4327, 2021.
- [6] Yuning You, Tianlong Chen, Yongduo Sui, Ting Chen, Zhangyang Wang, and Yang Shen. Graph contrastive learning with augmentations. *Advances in Neural Information Processing Systems*, 33:5812–5823, 2020.
- [7] Jun Xia, Lirong Wu, Jintao Chen, Bozhen Hu, and Stan Z Li. Simgrace: A simple framework for graph contrastive learning without data augmentation. In *Proceedings of the ACM Web Conference 2022*, pages 1070–1079, 2022.
- [8] Zhenyu Hou, Xiao Liu, Yukuo Cen, Yuxiao Dong, Hongxia Yang, Chunjie Wang, and Jie Tang. Graphmae: Self-supervised masked graph autoencoders. In *Proceedings of the 28th ACM SIGKDD Conference on Knowledge Discovery and Data Mining*, pages 594–604, 2022.
- [9] Jacob Devlin, Ming-Wei Chang, Kenton Lee, and Kristina Toutanova. Bert: Pre-training of deep bidirectional transformers for language understanding. *arXiv preprint arXiv:1810.04805*, 2018.
- [10] X Chen, S Xie, and K He. An empirical study of training self-supervised vision transformers. in 2021 ieee. In *CVF International Conference on Computer Vision (ICCV)*, pages 9620–9629, 2021.
- [11] Kaiming He, Xinlei Chen, Saining Xie, Yanghao Li, Piotr Dollár, and Ross Girshick. Masked autoencoders are scalable vision learners. In *Proceedings of the IEEE/CVF conference on computer vision and pattern recognition*, pages 16000–16009, 2022.
- [12] Chen Wei, Haoqi Fan, Saining Xie, Chao-Yuan Wu, Alan Yuille, and Christoph Feichtenhofer. Masked feature prediction for self-supervised visual pre-training. In *Proceedings of the IEEE/CVF Conference on Computer Vision and Pattern Recognition*, pages 14668–14678, 2022.
- [13] Jungwon Choi, Seongho Keum, EungGu Yun, Byung-Hoon Kim, and Juho Lee. A generative self-supervised framework using functional connectivity in fmri data. In *Temporal Graph Learning Workshop@ NeurIPS 2023*, 2023.
- [14] Mahmoud Assran, Quentin Duval, Ishan Misra, Piotr Bojanowski, Pascal Vincent, Michael Rabbat, Yann LeCun, and Nicolas Ballas. Self-supervised learning from images with a joint-embedding predictive architecture. In *Proceedings of the IEEE/CVF Conference on Computer Vision and Pattern Recognition*, pages 15619–15629, 2023.
- [15] Yujun Yan, Jiong Zhu, Marlina Duda, Eric Solarz, Chandra Sripada, and Danai Koutra. Groupinn: Grouping-based interpretable neural network for classification of limited, noisy brain data. In *Proceedings of the 25th ACM SIGKDD international conference on knowledge discovery & data mining*, pages 772–782, 2019.

- [16] Xiaoxiao Li, Yuan Zhou, Nicha Dvornek, Muhan Zhang, Siyuan Gao, Juntang Zhuang, Dustin Scheinost, Lawrence H Staib, Pamela Ventola, and James S Duncan. Braingnn: Interpretable brain graph neural network for fmri analysis. *Medical Image Analysis*, 74:102233, 2021.
- [17] Xuan Kan, Hejie Cui, Joshua Lukemire, Ying Guo, and Carl Yang. Fbnetgen: Task-aware gnn-based fmri analysis via functional brain network generation. In *International Conference on Medical Imaging with Deep Learning*, pages 618–637. PMLR, 2022.
- [18] Mingliang Wang, Jiashuang Huang, Mingxia Liu, and Daoqiang Zhang. Modeling dynamic characteristics of brain functional connectivity networks using resting-state functional mri. *Medical image analysis*, 71:102063, 2021.
- [19] Lingwen Liu, Guangqi Wen, Peng Cao, Tianshun Hong, Jinzhu Yang, Xizhe Zhang, and Osmar R Zaiane. Braintgl: A dynamic graph representation learning model for brain network analysis. *Computers in Biology and Medicine*, 153:106521, 2023.
- [20] Petar Veličković, William Fedus, William L Hamilton, Pietro Liò, Yoshua Bengio, and R Devon Hjelm. Deep graph infomax. *arXiv preprint arXiv:1809.10341*, 2018.
- [21] Junliang Yu, Hongzhi Yin, Xin Xia, Tong Chen, Lizhen Cui, and Quoc Viet Hung Nguyen. Are graph augmentations necessary? simple graph contrastive learning for recommendation. In *Proceedings of the 45th international ACM SIGIR conference on research and development in information retrieval*, pages 1294–1303, 2022.
- [22] Thomas N Kipf and Max Welling. Variational graph auto-encoders. *arXiv preprint arXiv:1611.07308*, 2016.
- [23] Alexander Schaefer, Ru Kong, Evan M Gordon, Timothy O Laumann, Xi-Nian Zuo, Avram J Holmes, Simon B Eickhoff, and BT Thomas Yeo. Local-global parcellation of the human cerebral cortex from intrinsic functional connectivity mri. *Cerebral cortex*, 28(9):3095–3114, 2018.
- [24] Junyoung Chung, Caglar Gulcehre, KyungHyun Cho, and Yoshua Bengio. Empirical evaluation of gated recurrent neural networks on sequence modeling. *arXiv preprint arXiv:1412.3555*, 2014.
- [25] Jean-Bastien Grill, Florian Strub, Florent Altché, Corentin Tallec, Pierre Richemond, Elena Buchatskaya, Carl Doersch, Bernardo Avila Pires, Zhaohan Guo, Mohammad Gheshlaghi Azar, et al. Bootstrap your own latent—a new approach to self-supervised learning. *Advances in Neural Information Processing Systems*, 33:21271–21284, 2020.
- [26] Ilya O Tolstikhin, Neil Houlsby, Alexander Kolesnikov, Lucas Beyer, Xiaohua Zhai, Thomas Unterthiner, Jessica Yung, Andreas Steiner, Daniel Keysers, Jakob Uszkoreit, et al. Mlp-mixer: An all-mlp architecture for vision. *Advances in Neural Information Processing Systems*, 34:24261–24272, 2021.
- [27] Qiaoyu Tan, Ninghao Liu, Xiao Huang, Rui Chen, Soo-Hyun Choi, and Xia Hu. Mgae: Masked autoencoders for self-supervised learning on graphs. *arXiv preprint arXiv:2201.02534*, 2022.
- [28] Cathie Sudlow, John Gallacher, Naomi Allen, Valerie Beral, Paul Burton, John Danesh, Paul Downey, Paul Elliott, Jane Green, Martin Landray, et al. Uk biobank: an open access resource for identifying the causes of a wide range of complex diseases of middle and old age. *PLoS medicine*, 12(3):e1001779, 2015.
- [29] Betty Jo Casey, Tariq Cannonier, May I Conley, Alexandra O Cohen, Deanna M Barch, Mary M Heitzeg, Mary E Soules, Theresa Teslovich, Danielle V Dellarco, Hugh Garavan, et al. The adolescent brain cognitive development (abcd) study: imaging acquisition across 21 sites. *Developmental cognitive neuroscience*, 32:43–54, 2018.
- [30] HCP WU-Minn. 1200 subjects data release reference manual. URL <https://www.humanconnectome.org>, 565, 2017.
- [31] Susan Y Bookheimer, David H Salat, Melissa Terpstra, Beau M Ances, Deanna M Barch, Randy L Buckner, Gregory C Burgess, Sandra W Curtiss, Mirella Diaz-Santos, Jennifer Stine Elam, et al. The lifespan human connectome project in aging: an overview. *Neuroimage*, 185:335–348, 2019.
- [32] Leah H Somerville, Susan Y Bookheimer, Randy L Buckner, Gregory C Burgess, Sandra W Curtiss, Mirella Dapretto, Jennifer Stine Elam, Michael S Gaffrey, Michael P Harms, Cynthia Hodge, et al. The lifespan human connectome project in development: A large-scale study of brain connectivity development in 5–21 year olds. *Neuroimage*, 183:456–468, 2018.
- [33] Kathryn E Lewandowski, Sylvain Bouix, Dost Ongur, and Martha E Shenton. Neuroprogression across the early course of psychosis. *Journal of Psychiatry and Brain Science*, 5, 2020.
- [34] Cameron Craddock, Yassine Benhajali, Carlton Chu, Francois Chouinard, Alan Evans, András Jakab, Budhachandra Singh Khundrakpam, John David Lewis, Qingyang Li, Michael Milham, et al. The neuro bureau preprocessing initiative: open sharing of preprocessed neuroimaging data and derivatives. *Frontiers in Neuroinformatics*, 7(27): 5, 2013.

-
- [35] Matthew RG Brown, Gagan S Sidhu, Russell Greiner, Nasimeh Asgarian, Meysam Bastani, Peter H Silverstone, Andrew J Greenshaw, and Serdar M Dursun. Adhd-200 global competition: diagnosing adhd using personal characteristic data can outperform resting state fmri measurements. *Frontiers in systems neuroscience*, 6:69, 2012.
- [36] Andrew R Mayer, David Ruhl, Flannery Merideth, Josef Ling, Faith M Hanlon, Juan Bustillo, and Jose Canive. Functional imaging of the hemodynamic sensory gating response in schizophrenia. *Human brain mapping*, 34(9): 2302–2312, 2013.
- [37] Felix L Opolka, Aaron Solomon, Cătălina Cangea, Petar Veličković, Pietro Liò, and R Devon Hjelm. Spatio-temporal deep graph infomax. *arXiv preprint arXiv:1904.06316*, 2019.
- [38] Keyulu Xu, Weihua Hu, Jure Leskovec, and Stefanie Jegelka. How powerful are graph neural networks? *International Conference on Learning Representations*, 2019.
- [39] AA Leman and Boris Weisfeiler. A reduction of a graph to a canonical form and an algebra arising during this reduction. *Nauchno-Technicheskaya Informatsiya*, 2(9):12–16, 1968.
- [40] Jie Hu, Li Shen, and Gang Sun. Squeeze-and-excitation networks. In *Proceedings of the IEEE conference on computer vision and pattern recognition*, pages 7132–7141, 2018.
- [41] Dan Hendrycks and Kevin Gimpel. Gaussian error linear units (gelus). *arXiv preprint arXiv:1606.08415*, 2016.
- [42] Jimmy Lei Ba, Jamie Ryan Kiros, and Geoffrey E Hinton. Layer normalization. *arXiv preprint arXiv:1607.06450*, 2016.
- [43] Guillaume Alain and Yoshua Bengio. Understanding intermediate layers using linear classifier probes. *arXiv preprint arXiv:1610.01644*, 2016.
- [44] Li Jing, Pascal Vincent, Yann LeCun, and Yuandong Tian. Understanding dimensional collapse in contrastive self-supervised learning. *International Conference on Learning Representations*, 2021.
- [45] Kartik Gupta, Thalaisyasingam Ajanthan, Anton van den Hengel, and Stephen Gould. Understanding and improving the role of projection head in self-supervised learning. *arXiv preprint arXiv:2212.11491*, 2022.
- [46] Diederik P Kingma and Max Welling. Auto-encoding variational bayes. *arXiv preprint arXiv:1312.6114*, 2013.
- [47] Bryan Perozzi, Rami Al-Rfou, and Steven Skiena. Deepwalk: Online learning of social representations. In *Proceedings of the 20th ACM SIGKDD international conference on Knowledge discovery and data mining*, pages 701–710, 2014.

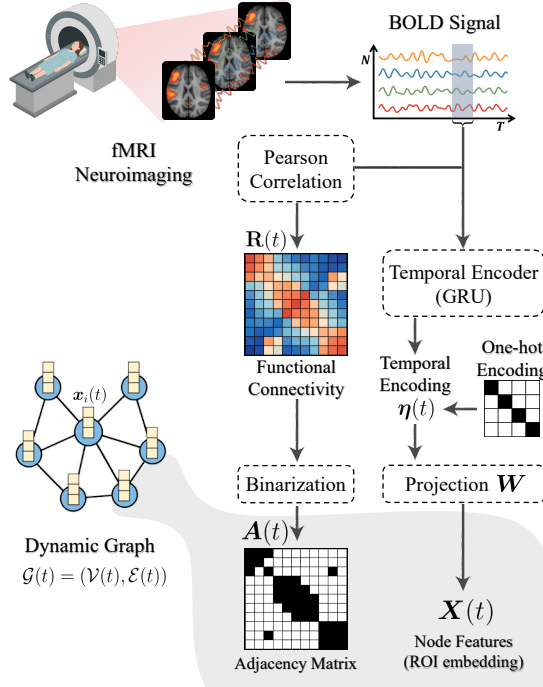


Figure 3: Overview of dynamic graph construction from fMRI data.

A Algorithmic Flow of ST-JEMA

To further facilitate understanding, we summarized the overall pipeline of our proposed Spatio-Temporal Joint Embedding Masked Autoencoder (ST-JEMA) framework for self-supervised learning on fMRI data in Algorithm 1. The algorithm describes the spatial and temporal reconstruction process of node representations and adjacency matrices employing K block masks, assuming the initial conversion of fMRI BOLD signals \mathbf{P} into dynamic graphs $\mathcal{G}(t)$ has already been completed. Detailed explanations of each equation and the methodological underpinnings can be found in Section 4.

B Constructing Dynamic Graphs from fMRI data

fMRI data are complex and multidimensional, consisting of a sequence of brain images represented in 3D voxels collected over time. Each voxel within these images stands for a tiny volume in the brain, and the value of each voxel reflects the intensity of the BOLD signal at that particular location and time. In this study, we focus on neural activity within predefined ROI, Schaefer atlas [23], leveraging its comprehensive partitioning of the cerebral cortex into functionally homogeneous regions. We construct the ROI-based BOLD signal data matrix $\mathbf{P} \in \mathbb{R}^{N \times T_{max}}$, with N representing the number of ROI and T_{max} the time points, by averaging BOLD signals within each ROI. This simplification retains essential details for subsequent dynamic functional connectivity analysis.

To analyze the BOLD signal with GNN, we construct dynamic graphs from the ROI-time-series matrix \mathbf{P} of resting state fMRI (rs-fMRI) by defining node features \mathbf{X} and the adjacency matrix \mathbf{A} . In this study, we utilize rs-fMRI because it allows for the exploration of spontaneous brain activity in the absence of task performance, offering insights into the brain’s intrinsic functional connectivity from understanding fundamental brain networks to predicting phenotypes such as gender or disease presence. For node feature \mathbf{X} , the ROI-time-series matrix \mathbf{P} serves as the basis for generating node features that capture their temporal dynamics. Each node features \mathbf{x} is combined spatial embeddings with learned temporal encodings using concatenation operation \parallel . Specifically, the feature vector of i -th node at time t is formulated as:

$$\mathbf{x}_i(t) = \mathbf{W}[\mathbf{e}_i \parallel \boldsymbol{\eta}(t)], \quad (27)$$

where $\mathbf{W} \in \mathbb{R}^{d_v \times (N+d_\eta)}$ is a learnable parameter matrix, \mathbf{e}_i denotes the one-hot spatial embedding of the i -th node, and $\boldsymbol{\eta}(t) \in \mathbb{R}^{d_\eta}$ is the temporal encoding obtained through a Gated Recurrent Unit (GRU) [24]. Here, d_η refers to the

Algorithm 1 Spatio-Temporal Joint Embedding Masked Autoencoder (ST-JEMA)

```

1: Input: Node features  $\mathbf{X}(t)$ , Adjacency matrix  $\mathbf{A}(t)$  where  $t \in [T_G]$ , the number of times for dynamic graphs  $T_G$ , minimum
   and maximum masking size ratio of nodes  $(\alpha_{\min}, \alpha_{\max})$ , the number of node  $N$ , window length  $\Gamma$ , window stride  $S$ , the ratio of
   spatial reconstruction factor  $\gamma$ , node reconstruction weight  $\lambda_{\text{node}}$ , and edge reconstruction weight  $\lambda_{\text{adj}}$ .
2: Output: pretrained target GNN encoder  $f(\cdot; \bar{\theta})$ 
3: Initialize context encoder  $f_{\text{cxt}}$ , target encoder  $f_{\text{tar}}$ , node decoder  $g_{\text{node}}$  and edge decoder  $g_{\text{edge}}$ .
4: for each step do
5:    $\mathcal{L}_{\text{spat}} \leftarrow 0$  and  $\mathcal{L}_{\text{temp}} \leftarrow 0$  ▷ Initialize losses for each step
6:   for  $t \in \mathcal{T}$  do
7:     /* Block masking process */
8:     Sample  $K$  Block Masks  $\mathbf{M}_{\mathbf{X}}(t), \mathbf{M}_{\mathbf{A}}(t)$  with  $\alpha(t) \sim \text{Uniform}(\alpha_{\min}, \alpha_{\max})$ .
9:      $\mathbf{X}_{\text{cxt}}(t), \mathbf{A}_{\text{cxt}}(t) \leftarrow \text{Block Masking}(\mathbf{X}(t), \mathbf{A}(t), \mathbf{M}_{\mathbf{X}}(t), \mathbf{M}_{\mathbf{A}}(t))$ 
10:     $\mathbf{Z}(t) \leftarrow f_{\text{cxt}}(\mathbf{X}_{\text{cxt}}(t), \mathbf{A}_{\text{cxt}}(t); \theta)$ 
11:     $\mathbf{Z}_{\text{tar}}(t) \leftarrow f_{\text{tar}}(\mathbf{X}(t), \mathbf{A}(t); \bar{\theta})$ 
12:    /* Encode context and target node features */
13:     $\mathbf{Z}(t) \leftarrow f_{\text{cxt}}(\mathbf{X}_{\text{cxt}}(t), \mathbf{A}_{\text{cxt}}(t); \theta)$ 
14:     $\mathbf{Z}_{\text{tar}}(t) \leftarrow f_{\text{tar}}(\mathbf{X}(t), \mathbf{A}(t); \bar{\theta})$ 
15:    /* Spatial reconstruction */
16:     $\tilde{\mathbf{Z}} \leftarrow \mathbf{W}_S^V \mathbf{Z}(t)$ 
17:     $\tilde{\mathbf{Z}}_{\text{cxt}}(t) \leftarrow \tilde{\mathbf{Z}} \odot \bigcap_{k=1}^K \mathbf{M}_{\mathbf{X}}^{(k)}(t)$ 
18:     $\mathbf{H}(t) \leftarrow g_{\text{edge}}(\mathbf{W}_S^E \mathbf{Z}(t); \phi_E)$ 
19:     $\hat{\mathbf{A}}(t) = \text{sig}(\mathbf{H}(t)\mathbf{H}(t)^\top)$ 
20:    for  $k \in [K]$  do
21:       $\tilde{\mathbf{Z}}_{\text{cxt}}^{(k)}(t) \leftarrow \tilde{\mathbf{Z}}_{\text{cxt}}(t) + \mathbf{m} \cdot (\mathbf{1}_{\mathbf{X}} - \mathbf{M}_{\mathbf{X}}^{(k)}(t))$ 
22:       $\tilde{\mathbf{Z}}_{\text{tar}}^{(k)}(t) \leftarrow g_{\text{node}}(\tilde{\mathbf{Z}}_{\text{cxt}}^{(k)}(t); \phi_V)$ 
23:       $\mathcal{L}_{\text{node-spat}}^{(t)} \leftarrow \frac{1}{K} \sum_{k \in [K]} \mathcal{L}_{\text{MSE}}(\tilde{\mathbf{Z}}_{\text{tar}}^{(k)}(t), \mathbf{Z}_{\text{tar}}^{(k)}(t))$  ▷ Spatial node latent reconstruction
24:       $\mathcal{L}_{\text{adj-spat}}^{(t)} \leftarrow \frac{1}{K} \sum_{k \in [K]} \mathcal{L}_{\text{BCE}}(\hat{\mathbf{A}}_{\text{tar}}^{(k)}(t), \mathbf{A}_{\text{tar}}^{(k)}(t))$  ▷ Spatial adjacency matrix reconstruction
25:    end for
26:     $\mathcal{L}_{\text{spat}}^{(t)} = \lambda_{\text{node}} \mathcal{L}_{\text{node-spat}}^{(t)} + \lambda_{\text{adj}} \mathcal{L}_{\text{adj-spat}}^{(t)}$ 
27:     $\mathcal{L}_{\text{spat}} = \mathcal{L}_{\text{spat}} + \mathcal{L}_{\text{spat}}^{(t)}$  ▷ Aggregate spatial reconstruction loss.
28:    /* Temporal reconstruction */
29:    Sample  $t_a \stackrel{\text{i.i.d.}}{\sim} U_{\text{int}}([0, t - \frac{1}{2}(\frac{\Gamma}{S} + 1)])$ ,  $t_b \stackrel{\text{i.i.d.}}{\sim} U_{\text{int}}([t + \frac{1}{2}(\frac{\Gamma}{S} + 1), T_G])$ .
30:     $\tilde{\mathbf{Z}}_{a,b}(t) \leftarrow \mathbf{W}_T [\tilde{\mathbf{Z}}(t_a) \parallel \tilde{\mathbf{Z}}(t_b)]$ 
31:     $\bar{\mathbf{A}}_{\text{tar}}(t) = \frac{1}{2} (\text{sig}(\mathbf{H}(t_a)\mathbf{H}(t_b)^\top) + \text{sig}(\mathbf{H}(t_b)\mathbf{H}(t_a)^\top))$ 
32:    for  $k \in [K]$  do
33:       $\bar{\mathbf{Z}}_{\text{cxt}}^{(k)}(t) \leftarrow \tilde{\mathbf{Z}}_{\text{cxt}}(t) + \tilde{\mathbf{Z}}_{a,b}(t) \odot (\mathbf{1}_{\mathbf{X}} - \mathbf{M}_{\mathbf{X}}^{(k)}(t))$ 
34:       $\mathcal{L}_{\text{node-temp}}^{(t)} \leftarrow \frac{1}{K} \sum_{k \in [K]} \mathcal{L}_{\text{MSE}}(\bar{\mathbf{Z}}_{\text{tar}}^{(k)}(t), \mathbf{Z}_{\text{tar}}^{(k)}(t))$  ▷ Temporal node latent reconstruction
35:       $\mathcal{L}_{\text{adj-temp}}^{(t)} = \frac{1}{K} \sum_{k \in [K]} \mathcal{L}_{\text{BCE}}(\bar{\mathbf{A}}_{\text{tar}}^{(k)}(t), \mathbf{A}_{\text{tar}}^{(k)}(t))$  ▷ Temporal adjacency matrix reconstruction
36:    end for
37:     $\mathcal{L}_{\text{temp}}^{(t)} \leftarrow \lambda_{\text{node}} \mathcal{L}_{\text{node-temp}}^{(t)} + \lambda_{\text{adj}} \mathcal{L}_{\text{adj-temp}}^{(t)}$ 
38:     $\mathcal{L}_{\text{temp}} \leftarrow \mathcal{L}_{\text{temp}} + \mathcal{L}_{\text{temp}}^{(t)}$  ▷ Aggregate temporal reconstruction loss.
39:  end for
40:   $\mathcal{L}_{\text{ST-JEMA}} = \gamma \mathcal{L}_{\text{spat}} + (1 - \gamma) \mathcal{L}_{\text{temp}}$ ,
41:  Update  $\theta, \phi_V$  and  $\phi_E$  by taking the gradient descent step with  $\mathcal{L}_{\text{ST-JEMA}}$ 
42:  Update  $\bar{\theta}$  using EMA based on  $\theta$ .
43: end for

```

Table 5: Phenotype information summary of the non-clinical and clinical rs-fMRI datasets

Dataset	Non-clinical					Clinical			
	UKB	ABCD	HCP-YA	HCP-D	HCP-A	HCP-EP	ABIDE	ADHD200	COBRE
No. Subjects	40913	9111	1093	632	723	176	884	668	173
Gender (F/M)	21 682 / 19 231	4370 / 4741	594 / 499	339 / 293	405 / 318	67 / 109	138 / 746	242 / 426	43 / 130
Age (Min-Max)	40.0-70.0	8.9-11.0	22.0-37.0	8.1-21.9	36.0-89.8	16.7-35.7	6.47-64.0	7.1-21.8	18.0-66.0
Diagnosis (P/C)	-	-	-	-	-	SPR 120 / 56	ASD 408 / 476	ADHD 280 / 389	BPD / SPR / SZA (9 / 69 / 11) / 84

dimensionality of the temporal encoding. This temporal encoding is designed to capture the dynamic changes in BOLD signals within each ROI over time, thus incorporating temporal variations into the node features. Now, the final node feature matrix $\mathbf{X}(t)$ can be defined as a stack of node feature vectors at time t :

$$\mathbf{X}(t) = \begin{bmatrix} | & & | \\ \mathbf{x}_1(t) & \cdots & \mathbf{x}_N(t) \\ | & & | \end{bmatrix}. \quad (28)$$

For the adjacency matrix $\mathbf{A}(t)$, we derive the FC between ROI based on the temporal correlation of BOLD signal changes, utilizing the ROI-timeseries matrix \mathbf{P} . The FC matrix at time t , $\mathbf{R}(t)$, is calculated as follows:

$$R_{ij}(t) = \frac{\text{Cov}(\bar{\mathbf{p}}_i(t), \bar{\mathbf{p}}_j(t))}{\sqrt{\text{Var}(\bar{\mathbf{p}}_i(t))\sqrt{\text{Var}(\bar{\mathbf{p}}_j(t))}} \in \mathbb{R}^{N \times N}, \quad (29)$$

where $\bar{\mathbf{p}}_i(t)$ and $\bar{\mathbf{p}}_j(t)$ are the BOLD signal vectors for nodes i and j within the temporal windowed matrix $\bar{\mathbf{P}}(t) \in \mathbb{R}^{N \times \Gamma}$ from \mathbf{P} , characterized by a temporal window length of Γ and stride S . Here, $t \in [T_G]$ where $T_G = \lfloor (T_{\max} - \Gamma) / S \rfloor$. Cov denotes the covariance, and Var represents the variance operation. The adjacency matrix $\mathbf{A}(t) \in \{0, 1\}^{N \times N}$ is then obtained by applying a threshold to the correlation matrix $\mathbf{R}(t)$, wherein the top 30-percentile values are considered as significant connections (1), and all others are considered as non-significant (0).

C Datasets

C.1 Data Preprocessing

We preprocessed all fMRI data to be registered with the standard Montreal Neurological Institute (MNI) space, ensuring consistency and comparability across datasets. The region of interest (ROI)-time-series matrices were extracted using the Schaefer atlas [23], which identifies 400 distinct ROIs within the brain for analyzing functional connectivity.

From the time-series BOLD signal \mathbf{P} in each fMRI dataset, we construct two types of graphs: a static graph and a dynamic graph. While the dynamic graph is constructed as described in Appendix B, for the static graph, we build the adjacency matrix \mathbf{A} to represent the functional connectivity of ROI by windowing across all time stamps $\tau \in [T_{max}]$. Additionally, the node feature \mathbf{X} is constructed using one-hot positional encoding, followed by a projection through the matrix \mathbf{W} .

C.2 Data Description

UK Biobank (UKB) [28]: We utilized 40 913 samples of resting-state fMRI from the UK Biobank, a comprehensive biomedical database of genetic, lifestyle, and health information from half a million participants. This dataset supports advanced medical research by offering insights into serious illnesses through diverse data collections, including genome sequencing, health record linkages, and functional MRI imaging.

Adolescent Brain Cognitive Development (ABCD) [29]: A longitudinal study tracking nearly 12 000 youth across 21 research sites to investigate the impact of childhood experiences on brain development and various behavioral, social, and health outcomes. We constructed 9,111 samples aged 9 to 11 years.

Human Connectome Project Young Adults (HCP-YA) [30]: Mapping the connectome of healthy individuals, this project provides a comprehensive database from 1200 young adults, incorporating advanced 3T and 7T MRI scanners for an exploration of brain connectivity and function. In our study, we specifically utilized rs-fMRI data from 1,093 subjects, following the pre-processing methodology described in Kim et al. [5].

Human Connectome Project Aging (HCP-A) [31]: Investigating the effects of aging on brain structure and function, this segment of the Human Connectome Project includes 1200 adults aged 36 to 100+ years. It aims to uncover how brain connections change with age in healthy individuals using a 3T MRI scanner. For our analysis, we utilized rs-fMRI data from 724 samples aged 36 to 89 years.

Human Connectome Project Development (HCP-D) [32]: This dataset includes over 1300 participants ranging from 5 to 21 years old, exploring the dynamics of brain development from childhood through adolescence using a 3T MRI scanner. Specifically, our study utilizes rs-fMRI data from 632 individuals aged between 8 and 21 years.

Human Connectome Project for Early Psychosis (HCP-EP) [33]: Focusing on early psychosis within the first three years of symptom onset, this dataset includes comprehensive imaging using a 3T MRI scanner, behavioral, clinical, cognitive, and genetic data from 400 subjects aged 16 to 35 years, including labels for schizophrenia (SPR). The objective is to identify disruptions in neural connections that underlie both brain function and dysfunction during a critical period with fewer confounds such as prolonged medication exposure. Our study employs rs-fMRI data from 176 subjects.

Autism Brain Imaging Data Exchange (ABIDE) [34]: This dataset gathers rs-fMRI, anatomical, and phenotypic data from 1112 individuals across 17 international sites, aiming to enhance the understanding of Autism Spectrum Disorder (ASD) through collaborative research. For our study, we specifically utilized rs-fMRI data from 884 individuals, ranging in age from 6 to 64 years.

ADHD200 [35]: This dataset initiative advances Attention Deficit Hyperactivity Disorder (ADHD) research by offering unrestricted access to 776 resting-state fMRI and anatomical datasets of individuals aged from 7 to 21 years, which includes 285 subjects with ADHD and 491 typically developing controls, from 8 international imaging sites. In our study, we utilized rs-fMRI data from 668 subjects.

The Center for Biomedical Research Excellence (COBRE) [36]: We constructed rs-fMRI datasets comprising 173 samples, including 84 patients with schizophrenia (SPR), 9 with bipolar disorder (BPD), 11 with schizoaffective disorder (SZA), and 75 healthy controls, ranging in age from 18 to 66 years. This dataset aims to facilitate the exploration of neural mechanisms underlying various mental illnesses.

D Competing Methods

To compare with our proposed ST-JEMA, we evaluated eight competing algorithms, each designed for pre-training GNN encoders using SSL methods, excluding Random-Init:

Random-Init: Training from scratch on the downstream dataset without the pre-training step using the upstream dataset. We present two sets of results for Random-Init, specifically when using a static graph as input and a dynamic graph as input, as elaborated in Appendix C.1.

DGI [20]: A contrastive SSL method for static graph data that learns mutual information between node and graph representations.

SimGRACE [7]: A contrastive SSL method for static graph data that utilizes model parameter perturbation to generate different views instead of using graph augmentations.

GAE [22]: A generative SSL method for static graph data that utilizes an autoencoder framework. GAE reconstructs a graph’s original adjacency matrix by leveraging node representations.

VGAE [22]: A generative SSL method for static graph data that improves GAE by using a variational autoencoder in the encoder.

GraphMAE [8]: A generative SSL method for static graph data that focuses on node reconstruction with masked autoencoder loss.

ST-DGI [37]: A contrastive SSL method for dynamic graph data that enhances DGI by optimizing the mutual information between node embeddings $\mathbf{Z}(t)$ and features at future k -time steps $\mathbf{Z}(t+k)$.

ST-MAE [13]: A generative SSL method specifically designed for fMRI data. ST-MAE focuses on dynamic FC by utilizing a masked autoencoder framework that accounts for temporal dynamics.

E Experimental Details

In this section, we detail the implementation of the models for ST-JEMA and training pipelines for upstream and downstream datasets.

E.1 Architecture Details

In this research, we utilize a 4-layer Graph Isomorphism Network (GIN) [38] as the GNN encoder and the Squeeze-Excitation READOUT (SERO) readout module in the fine-tuning process following the approach introduced by Kim et al. [5]. To ensure that each decoder effectively reconstructs target components from context node representations, we employ MLP-Mixer [26] for both node and edge decoders. Here, we provide detailed architectural information about GIN, SERO, and MLP-Mixer.

Graph Isomorphism Network (GIN) [38]:

Graph Isomorphism Networks, are specialized spatial GNN optimized for graph classification, achieving performance comparable to the Weisfeiler-Lehman (WL) test [39]. The GIN architecture aggregates neighboring node features through summation and employs an MLP for feature transformation, enabling the learning of injective mappings. This unique structure enables GINs to adeptly capture complex graph patterns, proving particularly effective in analyzing fMRI data for tasks such as gender classification from rs-fMRI data [3]. The mathematical formulation of GIN at layer l is as follows:

$$\mathbf{z}_i^{(l)} = \text{MLP}^{(l)} \left((1 + \epsilon^{(l)}) \cdot \mathbf{z}_i^{(l-1)} + \sum_{j \in \mathcal{N}(i)} \mathbf{z}_j^{(l-1)} \right), \quad (30)$$

where $\epsilon^{(k)}$ is a parameter optimized during training. The application of GINs to fMRI data analysis marks a significant progression, offering refined insights into the spatial and temporal dynamics of brain activity.

Squeeze-Excitation READOUT (SERO) [5]: SERO is the noble readout module that adapts the concept of attention mechanisms from Squeeze-and-Excitation Networks [40], adjusting it to apply attention across the node dimension instead of the channel dimension for GNNs. This modification enhances the focus on the structural and functional properties of nodes within brain graphs. The attention mechanism is mathematically defined as follows:

$$\mathbf{a}_{\text{space}}(t) = \text{sig}(\mathbf{W}_2 \sigma(\mathbf{W}_1 \mathbf{Z}(t) \Phi_{\text{mean}})), \quad (31)$$

where $\Phi_{\text{mean}} = [1/N, \dots, 1/N]$ is a mean vector for mean pooling, $\mathbf{W}_1 \in \mathbb{R}^{d_{\text{enc}} \times d_{\text{enc}}}$, $\mathbf{W}_2 \in \mathbb{R}^{N \times d_{\text{enc}}}$ are learnable parameter matrices, and σ is the nonlinear activation function such as ReLU. Finally, The graph representation at time t is derived by applying attention weights $\mathbf{a}_{\text{space}}(t)$ to each node of $\mathbf{Z}(t)$, effectively weighting the importance of each node’s features in the overall graph representation as follows:

$$\mathbf{z}_G(t) = \mathbf{Z}(t) \mathbf{a}_{\text{space}}(t). \quad (32)$$

This readout $\mathbf{z}_G(t)$ is used when the model is fine-tuned on the downstream task. When integrated into the STA-GIN [5] framework, this module significantly enhances performance in gender and task classification on fMRI data, demonstrating advancements over existing models.

MLP-Mixer [26]: MLP-Mixer adopts a purely MLP-based architecture, diverging from conventional convolution and self-attention mechanisms, comprising of token-mixing and channel-mixing Multi-Layer Perceptrons (MLPs). In this setup, we utilize the token-mixing MLPs to encourage interactions among nodes, while the channel-mixing MLPs facilitates feature communication across the feature dimension of node representations. For a graph with node representations $\mathbf{Z} \in \mathbb{R}^{N \times D}$, where N is the number of nodes and D is the dimension of node features, the MLP-Mixer operates as follows:

$$\begin{aligned} \mathbf{Y}_{*,i} &= \mathbf{Z}_{*,i} + \mathbf{W}_2 \text{GELU}(\mathbf{W}_1 \text{LN}(\mathbf{Z}_{*,i})), \quad i = \{1, \dots, N\}, \\ \hat{\mathbf{Z}}_{j,*} &= \mathbf{Y}_{j,*} + \mathbf{W}_4 \text{GELU}(\mathbf{W}_3 \text{LN}(\mathbf{Y}_{j,*})), \quad j = \{1, \dots, D\}, \end{aligned} \quad (33)$$

where GELU [41] is a non-linear activation function and LN [42] is a layer normalization. And $\mathbf{W}_1 \in \mathbb{R}^{\bar{N} \times \bar{N}}$, $\mathbf{W}_2 \in \mathbb{R}^{N \times \bar{N}}$, $\mathbf{W}_3 \in \mathbb{R}^{\bar{D} \times \bar{D}}$, and $\mathbf{W}_4 \in \mathbb{R}^{D \times \bar{D}}$ are learnable parameters for each MLPs with hidden dimension of \bar{N} and \bar{D} . This adaptation allows the MLP-Mixer to ensure communication between nodes for the reconstruction of targeted node representations from the aggregated context of the graph.

E.2 Experimental Details

Dynamic Graph Construction Settings

For the upstream dataset in our SSL methods, we utilize the UKB dataset with a window size $\Gamma = 50$ and a window stride $S = 16$ for constructing dynamic graphs. We split the upstream dataset into train (80%) / validation (10%) / test (10%) partitions and selected the pre-trained model for each SSL method based on the best-performing upstream SSL task on the test dataset. For downstream tasks, we construct dynamic graphs from fMRI datasets such as ABCD, HCP-YA, HCP-A, HCP-D, and HCP-EP are processed with a window size of 50 and a stride of 16. For the ABIDE, ADHD200, and COBRE datasets, we use a window size of 16 and a stride of 3 for consistency of fMRI scanning time. Following the approach by Kim et al. [5], we also randomly sliced the time dimension of the ROI-time-series BOLD signal matrix P , setting dynamic lengths of 400 for UKB, HCP-A, HCP-D, and HCP-EP; 380 for ABCD; 600 for HCP-YA; 70 for ABIDE and ADHD200; and 120 for COBRE.

Training Configuration and Optimization

We optimize the GNN encoder in two stages: (1) self-supervised pretraining on the upstream dataset, and (2) supervised finetuning on downstream tasks.

Pre-training employed a cosine decay learning schedule over 10 000 steps with a batch size of 16. Fine-tuning optimized the encoder with the task-specific head, using orthogonal regularization and a one-cycle scheduler for 30 epochs with a batch size of 32. Dynamic graphs integrated a mean pooling module for final representation processing. Classification tasks used cross-entropy loss, while age regression utilized MSE loss with normalized age data. The training utilized AMD EPYC processors, with NVIDIA RTX A6000 for pre-training and GeForce RTX 3090 for fine-tuning and ablation studies.

Optimization hyperparameters include a learning rate of 1×10^{-4} for ST-DGI, 5×10^{-4} for ST-MAE, and 5×10^{-5} for other SSL methods, with a consistent weight decay of 1×10^{-4} in the pre-training phase. For finetuning, a learning rate of 5×10^{-4} is used for gender and psychiatric diagnosis classification tasks, and 1×10^{-3} for the age regression task, selecting the best-performing model within weight decays of $\{1 \times 10^{-3}, 5 \times 10^{-4}, 1 \times 10^{-4}\}$. For Random-Init, a learning rate of 1×10^{-3} and weight decay of 1×10^{-4} are used across all tasks.

Additional hyperparameters for each SSL method are summarized in Table 6.

Table 6: Additional hyperparameters used for each SSL method.

Method	Key Hyperparameters
SimGRACE	Perturbation scale $\eta = 1.0$
GraphMAE	Masking ratio $\alpha = \{30, 50, 70\}$ (%)
ST-DGI	Temporal steps $k = \{1, 3, 6\}$
ST-MAE	Masking ratio $\alpha = \{30, 50, 70\}$ (%)
ST-JEMA	Block mask $\alpha_{\min-\max} = 10-30$ (%), $\gamma = 0.5$, $\lambda_{\text{node}} = 1.0$, $\lambda_{\text{edge}} = \{10^{-3}, 10^{-4}, 10^{-5}, 10^{-6}\}$

F Additional Experiments

F.1 Linear Probing Performance

A technique that can indirectly reflect whether the representations acquired through SSL in the pre-training phase contain valuable information for the downstream task is to perform linear probing on the downstream task and measure its performance [43]. In this context, linear probing refers to the learning process wherein the pre-trained encoder module in the model is frozen, and training is conducted solely on the task-specific head $h(\cdot, \omega)$ using the downstream dataset.

According to the results in Table 7, ST-JEMA exhibited higher AUROC performance than ST-MAE, suggesting that ST-JEMA captures more semantically rich information beneficial for psychiatric diagnosis classification. On the contrary, ST-DGI, a SSL method based on contrastive learning, exhibited lower performance than generative approaches. This suggests that the representations learned by ST-DGI might not be as beneficial for psychiatric diagnosis classification tasks compared to generative-based SSL methods.

Table 7: Linear probing performance of psychiatric diagnosis classification. The performance is evaluated using the AUROC score, with higher scores indicating better performance.

Pre-training	AUROC (\uparrow)			
	HCP-EP	ABIDE	ADHD200	COBRE
ST-DGI	70.66	53.87	53.32	63.73
ST-MAE	70.78	55.09	52.66	63.97
ST-JEMA	72.97	58.30	54.44	66.39

Table 8: Multi-task learning performance on ABIDE and ADHD200 datasets. Here, (-) represents a degree of performance drop, and (+) indicates the degree of performance improvement compared to the performance in each single-task learning scenario.

Pre-training	ABIDE		
	Gender	Age	Diagnosis
	AUROC (\uparrow)	MAE (\downarrow)	AUROC (\uparrow)
ST-DGI	65.00 (-9.87)	4.24 (-0.08)	59.50 (-9.36)
ST-MAE	62.86 (-11.88)	4.11 (-0.01)	58.25 (-11.48)
ST-JEMA	65.60 (-9.78)	4.06 (+0.02)	66.10 (-5.39)
Pre-training	ADHD200		
	Gender	Age	Diagnosis
	AUROC (\uparrow)	MAE (\downarrow)	AUROC (\uparrow)
ST-DGI	60.06 (-7.98)	1.99 (-0.08)	55.61 (-0.85)
ST-MAE	60.98 (-10.03)	1.89 (-0.03)	50.45 (-6.32)
ST-JEMA	68.29 (-3.65)	1.91 (-0.05)	59.84 (+0.95)

F.2 Multi-task Learning Performance

To further verify that ST-JEMA learns more informative representations compared to other baseline models, we conduct a multi-task learning experiment. In this setting, we concurrently train on three distinct tasks – gender classification, age regression, and diagnosis classification – within each dataset. To facilitate the simultaneous training of these three tasks, we employ three separate task-specific heads and fine-tune the pre-trained encoder and task-specific heads concurrently, utilizing aggregated loss from the three tasks.

Table 8 clearly shows that ST-JEMA achieved the best performance across all tasks compared to other baselines except for the age regression task in the ADHD200 dataset. Notably, ST-JEMA exhibits the smallest overall performance decline for each task when compared to the performance in the single-task learning scenario, outperforming other baseline models. In particular, regarding the age regression task in the ABIDE dataset and diagnosis classification task in ADHD200, ST-JEMA demonstrates an improvement in performance in the multi-task learning scenario compared to its performance in the single-task learning scenario. These findings highlight that the pre-trained encoder in ST-JEMA has effectively captured mutual information beneficial for addressing diverse downstream tasks.

F.3 Robustness on Missing Data Scenarios

To further confirm that ST-JEMA successfully captured the temporal dynamics in dynamic FC of fMRI data, we perform ablation experiments on the scenario of temporal missing data for the downstream dataset. Here, the temporal missing data scenario refers to assuming that a certain portion of timesteps is missing from the original data for each sample. To create the missing part from the original downstream training data, we mask randomly selected timesteps in BOLD signal according to a predefined missing ratio. We conduct experiments on the psychiatric diagnosis classification task using the ABIDE dataset, adjusting the missing ratio from 30% to 90%. As demonstrated in Fig. 4, we observed a decline in fine-tuning performance through all methods as the missing ratio increased. This indicates that the loss of temporal flow hinders the accurate prediction of psychiatric disorders, highlighting the importance of learning temporal dynamics for precise predictions. While ST-DGI and ST-MAE exhibited significant performance drops as the missing ratio increased, ST-JEMA maintained relatively better classification performance even with 90% of the data missing along the time axis. This suggests that our proposed SSL method enables the model to effectively learn temporal

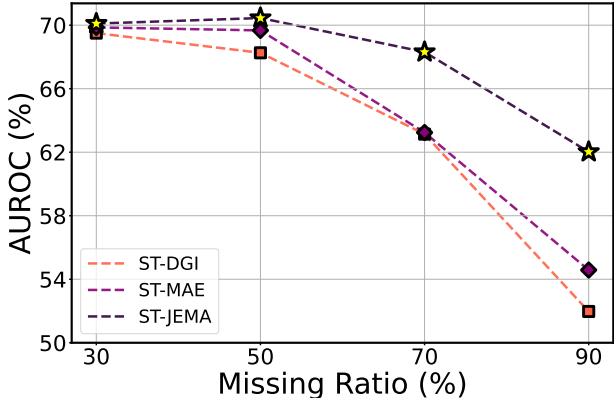


Figure 4: Ablation results on temporal missing data scenarios on psychiatric diagnosis classification task on ABIDE dataset. We designed temporal missing data scenarios by randomly masking the BOLD signal from fMRI data along the time axis, adjusting the missing ratio from 30% to 90%, and then measured the AUROC score to evaluate the effectiveness of SSL in capturing the temporal dynamics.

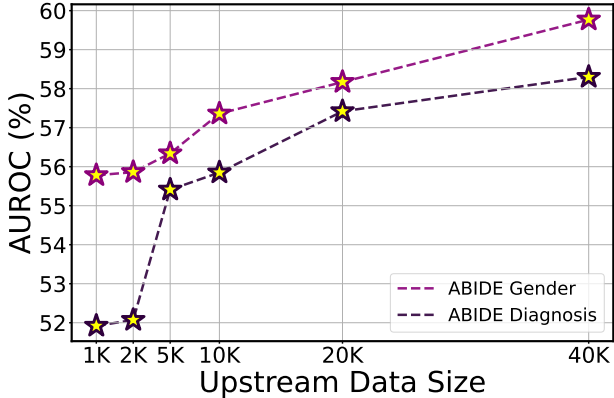


Figure 5: Ablation study on the impact of sample size for SSL on the ABIDE dataset. We evaluated learned representations for downstream tasks by training a linear probing model across varying numbers of samples.

dynamics, facilitating the learning of pre-trained representations useful for downstream tasks such as psychiatric diagnosis classification.

F.4 Impact of Pre-Training Data Size

To confirm the impact of the quantity of upstream UKB data on the quality of the pre-trained representation by the GNN encoder, we perform an ablation experiment by varying the size of the pre-training data. To systematically evaluate the impact of varying training data sizes on the effectiveness of pre-trained representations in solving downstream tasks, we conducted linear probing on the gender classification task and the diagnosis classification task using the ABIDE dataset. Notably, linear probing preserves the pre-trained representations even after the fine-tuning process which effectively shows the quality of pre-trained representations. Fig. 5 clearly indicates that the performance improves as the size of the training data increases. This result demonstrates that ST-JEMA successfully learns more meaningful representations as the training dataset size increases. It suggests that ST-JEMA is adept at acquiring high-quality representations from the extensive UKB upstream dataset.

F.5 Ablation on Block Mask Ratio

In the masking process of target points in ST-JEMA, selecting the appropriate block mask ratio is crucial. It is essential to strike a balance that ensures sufficient information for reconstructing the target representation, while also making the problem challenging enough to prevent the GNN encoder from learning trivial representations. To analyze the

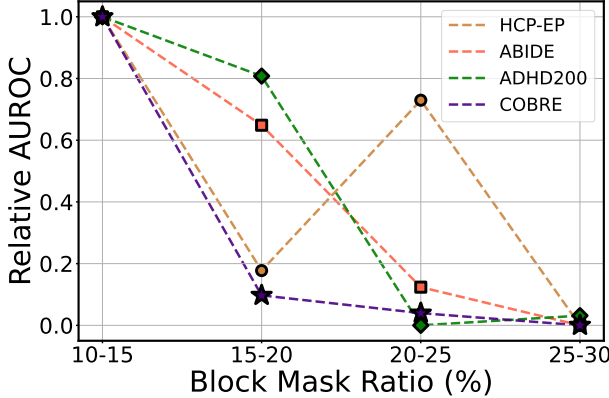


Figure 6: Ablation study on the block mask ratio of ST-JEMA for psychiatric diagnosis classification in clinical data. The x-axis, representing the block mask ratio, signifies the relative ratio of the minimum and maximum values within a specified range relative to the total size. The size of each block mask is randomly sampled from this range. To provide the outcomes across all datasets simultaneously, we present the relative AUROC results. Here, we calculate the relative AUROC by normalizing using the minimum and maximum AUROC results obtained from different block mask ratio ranges.

Table 9: Ablation results on different architecture for decoder module with diagnosis classification task on ABIDE dataset. The performance is evaluated using the AUROC score, with higher scores indicating better performance.

Decoder architecture	AUROC (\uparrow)
MLP	64.76
GIN [38]	66.35
MLP-Mixer [26]	71.49

appropriate block mask ratio in ST-JEMA, we perform an ablation experiment on the block mask ratio using the diagnosis classification task.

In Fig. 6, one can see that utilizing 10% ~ 15% is the optimal block mask ratio across all datasets. The trends are consistent across all datasets except for HCP-EP, where the performance improves with a block mask ratio of 20% ~ 25% compared to 15% ~ 20%. Since we employ 4 masks for each timestep $t \in [T_G]$, the optimal block mask ratio might change if the number of masks per each node and adjacency matrix is altered.

F.6 Decoder Architecture

As described in Section 4, We implemented the MLP-Mixer [26] to reconstruct the target node representation by integrating information from context node representations. Another approach to aggregate representations from different nodes is by using a GNN decoder. GraphMAE employed a more expressive GNN decoder instead of a simple MLP to prevent learning representations nearly identical to the low-level semantics of input features, thus aiming to capture higher-level semantics.

To determine which decoder structure is most effective for our methodology, we compared an MLP module, a one-layer GIN module, and a one-layer MLP-Mixer module. The MLP module does not utilize information from other node representations for reconstructing the target node and hence does not use a learnable token for node representation; instead, it reconstructs the target node representation using the corresponding node representation obtained from the GNN encoder. As seen in Table 9, the MLP decoder exhibited the lowest performance, possibly due to the pre-trained representations being of low-level semantics. While the GIN module performed better, its performance was similar to that of a random initialization, indicating limited benefit. In contrast, our method using the MLP-Mixer facilitated interactions among context node representations, thereby learning representations with higher-level semantics.

G Additional Related Works

G.1 Contrastive Self-supervised Learning on Graph

Contrastive methods focus on aligning representations derived from different ‘views’ of input graphs, known as positive pairs, typically generated through data augmentations or multiple snapshots of the same graph. The primary goal is to maximize the agreement between these positive pairs of samples, thereby enhancing the model’s ability to capture meaningful relationships within the data. To achieve this, a projection head is commonly employed to transform the encoder’s representations into an optimized feature space, enhancing discriminative power and learning stability while mitigating overfitting and preventing representation mode collapse [44, 45]. DGI [20] pioneered in graph contrastive SSL, aiming to maximize the mutual information between local and global graph representations. Subsequently, GraphCL [6] introduced graph augmentations to create different views for contrastive learning. However, the effectiveness of these augmentations can vary across different domains and sometimes restrict the graph structure. In response to these challenges, alternative strategies have been developed to bypass the need for complex augmentations. SimGCL [21] adopted a novel approach by adding noise to the embedding space to generate contrastive views, while SimGRACE [7] simplified the process by leveraging correlated views from perturbed GNN parameters.

G.2 Generative Self-supervised Learning on Graph

Generative approaches aim to reconstruct the original input by leveraging the encoded representations. Employing a decoder, these methods are tasked with reconstructing the original graph structure from the encoder’s embeddings. By optimizing the GNN model for precise reconstruction of the graph structure, generative methods enable the learning of representations that inherently capture the structural relationships in graph data. VGAE [22], a pioneer work in generative approach, introduces strategies to reconstruct a graph’s adjacency matrix from node embeddings. Utilizing variational autoencoders [46], VGAE demonstrates better performance in link prediction than conventional unsupervised learning methods. DeepWalk [47], highlighting their effectiveness in identifying important patterns in graph-structured data without labeled graph data. GraphMAE [8] adopts a novel approach to SSL in graph data by implementing a masked autoencoder for node feature reconstruction. GraphMAE demonstrates notable advantages over traditional contrastive learning techniques in tasks such as node and graph classification, showing evidence that generative self-supervised is also effective in the graph domain beyond the computer vision task.